

A FUSE survey of high-latitude Galactic molecular hydrogen

B.P. Wakker¹

ABSTRACT

Measurements of molecular hydrogen (H_2) column densities are presented for the first six rotational levels ($J=0$ to 5) for 73 extragalactic targets observed with *FUSE*. All of these have a final signal-to-noise ratio larger than 10, and are located at galactic latitude $|b| > 20^\circ$. The individual observations were calibrated with the *FUSE* calibration pipeline CalFUSE version 2.1 or higher, and then carefully aligned in velocity. The final velocity shifts for all the *FUSE* segments are listed. H_2 column densities or limits are determined for the 6 lowest rotational (J) levels for each H I component in the line of sight, using a curve-of-growth approach at low column densities (< 16.5), and Voigt-profile fitting at higher column densities. Detections include 65 measurements of low-velocity H_2 in the Galactic Disk and lower Halo. Eight sightlines yield non-detections for Galactic H_2 . The measured column densities range from $\log N(\text{H}_2)=14$ to $\log N(\text{H}_2)=20$. Strong correlations are found between $\log N(\text{H}_2)$ and T_{01} , the excitation temperature of the H_2 , as well as between $\log N(\text{H}_2)$ and the level population ratios ($\log(N(J')/N(J))$). The average fraction of nuclei in molecular hydrogen ($f(\text{H}_2)$) in each sightline is calculated; however, because there are many H I clouds in each sightline, the physics of the transition from H I to H_2 can not be studied. Detections also include H_2 in 16 intermediate-velocity clouds in the Galactic Halo (out of 35 IVCs). Molecular hydrogen is seen in one high-velocity cloud (the Leading Arm of the Magellanic Stream), although 19 high-velocity clouds are intersected; this strongly suggests that dust is rare or absent in these objects. Finally, there are five detections of H_2 in external galaxies.

Subject headings: ISM:general – ISM:molecules – Galaxy:disk – Galaxy:halo – ultraviolet:ISM

1. Introduction

Molecular hydrogen (H_2) is an important constituent of the interstellar medium (ISM), especially in the denser parts, where the presence of H_2 is connected with star formation.

¹Department of Astronomy, University of Wisconsin, 475 N. Charter St, Madison, WI 53706. Based on observations made with the NASA-CNES-CSA Far Ultraviolet Spectroscopic Explorer. *FUSE* is operated for NASA by the Johns Hopkins University under NASA contract NAS5-32985.

In its ground electronic state H_2 has many absorption lines in the ultraviolet part of the spectrum, between about 900 and 1130 Å. Using the *Copernicus* satellite, H_2 was detected in many sightlines toward nearby disk stars (Spitzer & Jenkins 1975, Savage et al. 1977), showing column densities between 10^{14} and 10^{20} cm^{-2} for sightlines with $N(\text{H I})$ below $\sim 5 \times 10^{21}$ cm^{-2} . At higher values of $N(\text{H I})$ a large fraction of the hydrogen becomes molecular. The formation of H_2 on interstellar dust particles is theoretically understood (Hollenbach et al. 1971). The transition from mostly neutral to mostly molecular to gas was worked out by Federman et al. (1979).

After *Copernicus* there was a long hiatus in the possibility of measuring interstellar H_2 . The *IMAPS* (Jenkins et al. 1988) and *ORFEUS* (Krämer et al. 1990) payloads on the *ASTRO-SPAS* space-shuttle platform provided $R=10^5$ and 10^4 resolution data in the 900–1100 Å spectral range, although for only a limited number of targets with V magnitudes <12 . The launch of the *Far Ultraviolet Spectroscopic Explorer (FUSE)* in 1999 resulted in much better access to the wavelength region containing the H_2 lines. The properties of the *FUSE* satellite have been described in detail by Moos et al. (2000) and Sahnou et al. (2000). The sensitivity of *FUSE* allows observing extragalactic and stellar background targets with fluxes down to about 10^{-14} $\text{erg cm}^{-2} \text{s}^{-1} \text{Å}^{-1}$ (corresponding to a V magnitude of about 16).

The molecular hydrogen lines in the FUV are associated with transitions from the ground electronic state, $X^1\Sigma_g^+$ to excited electronic states, $B^1\Sigma_u^+$ (Lyman bands) and $C^1\Pi_u$ (Werner bands). The transitions start from the ground ($v=0$) vibrational state and a range of rotational states, J . In practice transitions starting with $J=0$ to $J=5$ are observed. The even states ($J=0, 2, 4, \dots$) have a nuclear spin $S=0$ (para- H_2), while the odd states ($J=1, 3, 5, \dots$) have nuclear spin $S=1$ (ortho- H_2). Abgrall et al. (1993a, b) presented detailed tables of the wavenumbers and Einstein-A values for all these transitions. However, these are out of date, and this paper instead use the oscillator strengths, wavelengths and damping constants provided by Abgrall to the FUSE PI Team (courtesy of Ken Sembach).

The H_2 molecule provides some diagnostics of the physical conditions in the interstellar medium (see e.g. review by Shull & Beckwith 1982). The population ratios of the different rotational states can be described by a Boltzmann exponential ($N(J) \propto \exp(-E/kT)$). In practice, the Boltzmann temperatures are often just a convenient shorthand for describing the rotational level population ratios. However, the lowest of these temperatures (T_{01}) does provide a measure of the collisional excitation. In diffuse clouds, the higher rotational states are also excited by FUV radiation, and the populations of the higher J levels are governed by radiative excitation, followed by UV fluorescence, infrared radiative cascades and collisional de-excitation. These processes are described in several papers that discuss modeling of the population levels of H_2 in the diffuse ISM (see Browning et al. 2003 and many references therein, most usefully Spitzer & Zweibel 1974, Jura 1975a, b). In somewhat denser clouds the higher J -levels may also be collisionally excited, for which Gry et al. (2002) present some

evidence.

Toward almost all Galactic and extragalactic targets observed with *FUSE* Galactic low-velocity H₂ absorption is detected. Published studies include surveys of H₂ in diffuse clouds in the Milky Way, using disk OB stars (Rachford et al. 2002), in interstellar gas toward selected Seyferts and quasars (Sembach et al. 2001a, b), intermediate-velocity clouds (Richter et al. 2003), high-velocity clouds (Richter et al. 2001), the Magellanic Clouds (Tumlinson et al. 2003) and M33 (Bluhm et al. 2003).

As of 31 Dec 2004, *FUSE* has observed almost 400 extragalactic background targets (excluding LMC/SMC stars in this count). For 201 of these the signal-to-noise ratio (S/N) per 20 km s⁻¹ resolution element near 1030 Å is >3. However, for datasets with S/N<10, the H₂ becomes difficult to measure, and therefore this paper only includes the 73 targets with S/N>10. These targets are located at high galactic latitudes ($|b|>20^\circ$), and probe the diffuse H₂ in the Galactic Halo and the Disk near the Sun. They were originally observed for many different purposes, including the original survey of AGN sightlines by the *FUSE* Team aimed at measuring Galactic O VI absorption, high-velocity clouds and Galactic deuterium. Other targets come from general observer programs in *FUSE* Cycles 1 through 5, which include studies as diverse as searching for intergalactic O VI, measuring metals in Galactic high-velocity clouds and analyzing properties of starburst galaxies. The H₂ in these sightlines is often a contaminant for accomplishing the original aim of the observation. In fact, the current survey was started as a way to understand which features of interest might instead be H₂ and to be able to remove the H₂ lines. This paper therefore will concentrate on presenting the data analysis and the H₂ measurements, and only a minimal attempt is made at interpreting the results and discussing the implications for understanding the physical conditions of the Galactic ISM.

In Sect. 2 the observations are discussed. Section 3 presents the methods used to determine N(H₂), while Sect. 4 describes the results.

2. Observations and data reduction

2.1. The sightline sample

The sightlines in the sample are listed in Table 1. Columns 1, 2, 3 and 4 give the object name, galactic longitude and latitude, and the target type (QSO, Seyfert or Hubble type). Columns 5, 6 and 7 list the *FUSE* datasets, the version of the calibration pipeline that was used, and the exposure time. Many targets were observed multiple times. All these exposures and segments were combined before measuring the H₂ lines, in the manner discussed in Sect. 2.2 below. Each individual observation was obtained using the *FUSE* time-tag mode, almost always through the 30"×30" LWRS aperture. A note "3" to Col. 5 in Table 1 indicates the few datasets obtained through the 4"×20" MDRS aperture.

Each observation provides a photon list for each of a set of consecutive exposures corresponding to an orbital viewing period. The photon lists for each exposure are concatenated before being processed by the *FUSE* calibration pipeline. Wakker et al. (2003) provide a discussion of the steps involved in the calibration. However, they used the CalFUSE v1.8.7 version of the pipeline, which had some known problems, most notably an inaccurate wavelength scale. Later CalFUSE versions corrected this problem and also have better flux calibration, better modeling of event bursts, scattered light and astigmatism, error propagation, jitter correction and bad-pixel rejection. Therefore, we started recalibrating our old datasets with CalFUSE v2.1 as soon as it became available. When CalFUSE v2.4 became available, we switched to that version. In principle all datasets should have been recalibrated with CalFUSE v2.4, but due to lack of manpower and time about half are still v2.1. However, for the few cases where both v2.1 and v2.4 calibrations exist, there are no obvious differences between the two datasets.

The exposure times listed in Col. 7 of Table 1 are the nominal times listed in the *FUSE* observation log. Because of “bursts” (short-lasting large increases in the detector count rate) and passages through the South Atlantic Anomaly (SAA) as well as other such problems, part of the exposure may be unuseable. If the actual exposure time on either Side 1 or Side 2 of the detector is more than 10% less than the nominal time, the actual time is given in parentheses, with a note “1” or “2” indicating whether the loss of time pertains to Side 1 or Side 2.

2.2. Wavelength shifts

A *FUSE* spectrum consists of data for 8 detector segments, covering different, partially overlapping wavelength regions: LiF1A (987–1082 Å), LiF1B (1094–1187 Å), LiF2A (1085–1181 Å), LiF2B (983–1074 Å), SiC1A (1004–1091 Å), SiC1B (905–993 Å), SiC2A (917–1006 Å), SiC2B (1017–1105 Å). The sensitivity of the LiF1A and LiF2B segments is so much higher than that of SiC1A and SiC2B that the latter are rarely used. Similarly, the SiC2A data are of much better quality than those for SiC1B, so the SiC1B channel is ignored here. However, in the wavelength regions where they overlap, the S/N ratio provided by LiF2B/LiF1B is about half that of LiF1A/LiF2A, and it usually makes sense to combine the data for those segments, even though they have slightly different spectral resolutions. The SiC2B data cover a wavelength range similar to that of LiF1A and LiF2B, but they are much noisier and are only used in the wavelength region where they provide unique data (1082 to 1085 Å).

FUSE wavelengths are calibrated using a wavelength solution derived from a number of bright targets with well-studied and simple interstellar features (Sahnou et al. 2000). However, problems like minor misalignments in target positioning lead to zero point offsets

that are typically less than 10 km s^{-1} (half a resolution element, or 5 detector pixels), but which can be as large as 20 km s^{-1} . These offsets vary between different targets, sometimes between different observations of the same target taken at different times of the year, and also between different segments in the same observation. Offsets often occur for slightly extended sources, whose UV emission may peak at a different location than the optical position used to point the telescope. Correctly correcting for these offsets involves a major effort, without which absorption lines can be smeared and different segments and different exposures of the same target may end up misaligned.

Wakker et al. (2003) found shifts for the LiF1A and LiF2B segments by measuring the centroids of the interstellar Ar I-1048 and Si II-1020 lines, which span their line of interest – O VI $\lambda 1031.926$. This is insufficient for a study of H_2 , however. First, it is not a-priori true that the velocity of the H_2 is the same as that of the metal lines. This was demonstrated by Sembach et al. (2001b) in the sightline toward 3C 273.0, and it can also be seen by comparing the entries in Cols. 8 and 9 of Table 2. Second, shifts are needed for each detector segment, not just LiF1A/LiF2B. Third, for many sources the S/N ratio in each individual exposure is low and the centroids of the Ar I-1048 and Si II-1020 lines are difficult to determine.

A more rigorous approach is therefore taken in this paper. First, gaussians are fitted to an unshifted spectrum to find the centroids of all discernable metal and H_2 lines in each of the segments of each individual observation. In a number of sightlines intermediate-and/or high-velocity metal line absorption is seen, in which case separate centroid fits are made to these components. The metal lines usually include Si II $\lambda 1030.699$, Ar I $\lambda 1048.220$, Ar I $\lambda 1066.660$, Fe II $\lambda 1063.177$ for the LiF1A/LiF2B segments and Fe II $\lambda 1144.938$, 1121.975 , 1143.226 , 1125.448 , P II $\lambda 1152.818$ for the LiF1B/LiF2A segments. In many (but not all) sightlines, Fe II $\lambda 1081.875$, 1096.877 are also included (if not contaminated by H_2), and sometimes Fe II $\lambda 1055.262$, 1062.152 , 1063.972 , 1112.048 , 1127.098 , 1133.665 , 1142.366 (if strong enough). Occasionally O I $\lambda 1039.230$ and/or N I $\lambda 1134.165$, 1134.415 , 1134.980 are not contaminated by geocoronal emission and can be used. Metal lines uncontaminated by geocoronal emission are rare in the SiC2A segment, but selecting only the data taken during orbital night may allow measurements of O I $\lambda 948.686$, 936.630 , 976.448 , 929.517 , 950.885 , 924.952 , N I $\lambda 953.970$, 953.655 , 963.990 , 953.415 , 964.626 , 965.041 , and P II $\lambda 963.081$. Depending on the strength of the H_2 lines, anywhere between 0 and 40 H_2 lines can be discerned in any of the six analyzed segments. For sightlines with $\log N(\text{H}_2)=14\text{--}15$ several lines of $J=0$ and $J=1$ are strong and narrow enough to give reliable centroids. For $\log N(\text{H}_2)\sim 15\text{--}17$ lines for $J=2$ and $J=3$ and the weaker $J=0$ and $J=1$ lines are the most reliable. At higher $N(\text{H}_2)$ most of the $J=0$ and $J=1$ develop damping wings, and a centroid is no longer fitted. Lines that are blended with other H_2 or metal lines are not fitted either. The fitted centroids are then plotted against wavelength and separate average velocities are determined for the metal lines and the H_2 lines. The rms spread in the velocities ranges

from about 2 km s^{-1} for sightlines with high signal-to-noise ratio and simple absorption-line structure, to $6\text{--}8 \text{ km s}^{-1}$ for low signal-to-noise data.

For seven of the ten datasets in the sample that were obtained before 2 November 1999 (as well as for three later ones) a clear linear slope can be seen in the centroid vs wavelength plot for some (usually not all) segments, even after applying the v2.1.6 or v2.4.0 calibration. This slope is typically about 0.11 to $0.15 \text{ km s}^{-1}/\text{\AA}$, giving a total centroid shift of $\sim 20\text{--}30 \text{ km s}^{-1}$ across a segment. Not taking this into account would smear out H_2 lines at the edges of the segment and lead to erroneous equivalent width measurements. The values for these special slopes can be found in Note 4 to Table 1.

Two methods were used to determine the expected velocity of the metal lines. Twenty-one sightlines have data taken with the E140M grating on the Space Telescope Imaging Spectrograph (*STIS*). This spectrograph has better velocity resolution than *FUSE* (6.5 km s^{-1} vs 20 km s^{-1}), and its wavelength calibration appears to be more reliable, due to the much smaller slit ($0''.2$) (see appendix in Tripp et al. 2005). *STIS* data are provided on a heliocentric wavelength scale, and a heliocentric to LSR correction needs to be applied. Centroids were fitted to the metal lines in the *STIS* wavelength range that show clean profiles, which can include N I $\lambda\lambda 1199.550, 1200.223, 1200.710$, S II $\lambda\lambda 1250.584, 1253.811, 1259.519$, Ni II $\lambda\lambda 1317.217, 1370.132, 1454.842$, Fe II $\lambda 1608.451$, and Al II $\lambda 1670.787$. In general, they show an rms spread of about $1\text{--}2 \text{ km s}^{-1}$. The centroids of the *FUSE* metal lines are then aligned with the velocity implied by the *STIS*-E140M data.

If no *STIS* E140M data are available, the velocity of the metal lines is compared to that of the 21-cm H I emission. If there are well-detected intermediate- or high-velocity components, these are used preferentially. The H I spectrum can come from one of three possible sources, as described by Wakker et al. (2003), who show these H I spectra: a) special observations with the Effelsberg 100-m dish for a limited number of sightlines, b) the Leiden-Dwingeloo Survey (LDS, Hartmann & Burton 1997), or c) the Villa Elisa or IAR Survey (Arnal et al. 2000). The assumption that the centroid of the metal lines aligns with the peak of the H I emission often turns out to be incorrect. For the 19 sightlines that have *STIS*-E140M data a comparison of $\langle v \rangle$ (*STIS*) and $\langle v \rangle$ (21-cm) yields a range of $\pm 10 \text{ km s}^{-1}$ for the difference in velocities, with an average difference of 2 km s^{-1} and an rms of 4 km s^{-1} . However, even if the absolute velocity of the metal lines will not be exactly right, the relative alignment of the different *FUSE* detector segments will be.

There are five sightlines (1H 0707–495, Mrk 1095, MS 0700.7+6338, NGC 1068 and PG 0844+349, see Col. 10 of Table 2), where the H I spectrum shows a very narrow, very bright low-velocity component superimposed on a broader profile. In these cases the velocity of the H_2 (rather than that of the metal lines) was aligned with this probably cold H I.

The implied shifts usually show distinct patterns. The shifts implied by the metal and H_2 lines are often similar for all LiF1 and LiF2 segments, or for all segments on Side 1

and Side 2, or even for all LiF segments. Shifts that were similar to within about 1σ were averaged to find the final implied shifts for those segments. Shifts that are clearly different from each other were averaged separately. The shifts implied for SiC2A and SiC2B are often very different from those implied for the LiF segments. For exposures with low S/N, the SiC2B data are often too noisy to discern the absorption lines, and the SiC2A shift is assumed.

After determining the shifts for all segments, the LiF1A+LiF2B and LiF2A+LiF1B data from different observations are combined. Then the centroids of the metal and H₂ lines are fitted again, to check whether the average centroid velocities are now indeed equal to those implied by the STIS or the 21-cm data. Another iteration is done if they are not. The final shifts for each segment are presented in Cols. 8 to 13 of Table 1. For several observations the LiF2B or LiF1B segment shows a much lower flux than LiF1A or LiF2A, and is ignored when combining the segments; in other cases one or more segments do not show any flux. The unused segments are indicated by a “–” in Table 1.

Column. 2 to 6 of Table 2 present fluxes and S/N ratios for each target, determined near four wavelengths: 1031, 1063, 977 and 1122 Å. These are representative of the LiF1A+LiF2B, LiF1A+LiF2B, SiC2A, and LiF2A+LiF1B data, respectively. Two values are given for the LiF1A+LiF2B data, since in some sightlines there is redshifted Lyman- β intrinsic to the background galaxy that lowers the flux and S/N ratio near 1031 Å compared to the overall values in the segment. This is also reflected in the flux value given in Col. 2, which is usually valid near 1031 Å, but is for near 1063 Å if a note (^a) is given. Measuring the S/N ratios is done by fitting a 1st, 2nd or 3rd order polynomial to the continuum within about ± 1500 km s⁻¹ of the selected wavelength, and then calculating the rms of the residual of the fit. This is compared with the error array given by the calibration software to make sure that the rms makes sense – the rms of the residual should not be smaller than the errors; it generally is not more than 20% larger. For a few high signal-to-noise sightlines (3C 273.0, Mrk 509, NGC 1705, NGC 4151, PKS2155–304) fixed-pattern noise limits the S/N ratio to slightly better than 30. For other high S/N sightlines (Mrk 279, Mrk 421, Mrk 817, Mrk 876, PG 0804+761, PG 1259+593) there are multiple slightly-differently-aligned exposures, reducing the fixed-pattern noise, and allowing and S/N > 30.

The H I, metal-line and H₂ velocities that were measured are given in Cols. 7 to 9 of Table 2. Column 7 lists the velocities of the H I components found in the 21-cm spectra, which can be found in Wakker et al. (2003). Column 8 shows the metal-line velocities that can be derived from the alignment method described above, while Col. 9 gives the implied H₂ velocity. The distribution of $v(\text{metal}) - v(\text{H}_2)$ has an average of 0.4 km s⁻¹, and a dispersion of 3.9 km s⁻¹. The largest differences (± 9 km s⁻¹) occur for PG 1259+593 and PG 1302–102. Column 10 shows how the different kinds of data were aligned. “E140M” means that there is *STIS* data from which $v(\text{metal})$ follows, and the *FUSE* and *STIS* metal lines can be aligned,

implying $v(\text{H}_2)$. In this case $v(\text{H I})$ can be different from $v(\text{metal})$. “21cm” in Col. 10 means that the *FUSE* metal lines were aligned with the 21-cm data. Finally, “21cm-H2” implies that it was assumed that the H_2 aligns with a bright, narrow component in the 21-cm H I spectrum.

3. Determination of H_2 parameters

After properly aligning and combining the individual observations and segments, the H_2 column densities for each rotational (J) level can be measured. This is done in several steps. 1) A piecewise global continuum is fit to the combined data. 2) For each J level the continuum-normalized absorption lines are displayed all at once, and lines that are not blended, confused, or too noisy are selected interactively. 3) For $\log N(J) < 15.8$, a curve-of-growth is used to determine the column density and estimate the b -value, while for $\log N(J) > 16.6$ a Voigt profile is fit to the damping wings; for $\log N(J)$ between these two values either method may be used. 4) The column densities of the up to five different J levels are compared and parametrized with five parameters: $N(\text{H}_2, \text{total})$, b , T_{01} , T_{23} , and T_{34} . 5) The parametrization can be turned into a theoretical absorption profile for each line, which is overlaid on the data, in order to make sure that it makes sense. Now follow comments on each of these steps.

1) *Continuum fitting.* In principle one could fit a local continuum to each individual H_2 absorption line, using e.g. a $\sim 1500 \text{ km s}^{-1}$ wide velocity range (with all continua spliced together). However, in practice this is prohibitively time-consuming. Therefore, 1st to 4th order Legendre polynomials (see Sembach & Savage 1992) were fitted to line-free regions over up to 30 \AA wide wavelength ranges.

2) *Line selection.* After normalizing, the lines for each J level are displayed (sorted by oscillator strength), and lines for which reliable equivalent widths can be derived are selected interactively. Lines that are always blended with interstellar metal lines are excluded, as are lines blended with other H_2 lines. Also excluded are lines that are blended with intergalactic absorption, intrinsic AGN lines, or geocoronal emission. For sightlines with $\text{S/N}(\text{SiC2A})$ less than about 8, all lines with $\lambda < 1000 \text{ \AA}$ are usually excluded. Displaying all lines of a single J -level at once allows a check on whether the progression from strong to weak lines conforms to expectations.

3) *Column density measurement.* If $N(J) < 10^{16} \text{ cm}^{-2}$, a χ^2 fit is made. First, equivalent widths are determined by direct summation of the absorption over a $\sim 25 \text{ km s}^{-1}$ velocity extent. A χ^2 value is then calculated for every combination of $\log N$ and b :

$$\chi^2 = \sum \frac{(\text{EW}_{\text{obs}} - \text{EW}_{\text{pred}}(N, b))^2}{\sigma(\text{EW})^2}. \quad (1)$$

Minimizing χ^2 gives a “best-fit” column density and b -value for each individual J -level.

Of course, the resulting column density strongly depends on the b -value. Due to noise, uncertainties in continuum placements, and the relatively small range in $f\lambda$ values for each J -level the best-fit b -value generally differs for the different J -levels. Further, at low column densities the equivalent widths are independent of b , while at intermediate column densities the derived value of N is very sensitive to b . Therefore, it is assumed that b is the same for each J -level, and the resulting column density is the one that gives the lowest value of χ^2 , given a fixed value of b . How b is determined is described in point 5) below.

A few papers have claimed evidence for an increase in b with J (Spitzer & Cochran 1973, Spitzer et al. 1974, Lacour et al. 2005). These authors determined curves-of-growth toward high signal-to-noise Copernicus and *FUSE* spectra of nearby disk stars with high H_2 column densities. Only a few of the spectra of the extragalactic targets in this paper have comparable S/N ratios, and they all show much lower H_2 column densities. Limiting the check to the 18 sightlines with S/N>25, reliable independent b values for multiple J levels can be determined for just two H_2 components: $J=1$ to 3 at +28 km s⁻¹ toward 3C 273.0 and $J=0$ to 2 in the IVC toward PG 1116+215. The following FWHMs are found for 3C 273.0; FWHM($J=1$)=8.0±1.1, FWHM($J=2$)=7.7±1.3, FWHM($J=3$)=7.0±1.4; for PG 1116+215: FWHM($J=0$)=6.6±1.4, FWHM($J=1$)=7.0±1.4, FWHM($J=2$)=5.0±2.5. Thus, these two sightlines do not show clear evidence for systematic variations of the FWHM with J .

The determination of column densities is complicated by the fact that the $f\lambda$ values of the H_2 lines of a given level span only a relatively narrow range. For $J=0$, and $\lambda>1000$ Å, just seven lines are unblended, and the five strongest differ by just a factor 2.3 in $f\lambda$; the two most important lines are therefore L(1-0) R(0) λ 1092.195, and L(0-0) R(0) λ 1108.127, which are 4.8 and 16.6 times weaker than the strongest $J=0$ line. For $J=1$ the situation is slightly better, with 13 useful lines spanning a factor 6 in $f\lambda$, and two lines whose strength is 1/12.3 and 1/20.3 that of the strongest lines (L(1-0) P(1) λ 1094.052, L(0-0) R(1) λ 1108.633). For $J=2$ 15 lines span a factor 6.5 in $f\lambda$, with one more (L(1-0) P(2) λ 1096.44) 1/10.4 times the strength of the strongest. Thirteen $J=3$ lines span a factor 2.5 in $f\lambda$, with two substantially weaker lines (L(1-0) P(3) λ 1099.787 and L(0-0) P(3) λ 1115.895) factors of 7.6 and 26 below the strongest line. If $J=4$ or $J=5$ is detected, even the strongest lines are on the linear part of the curve-of-growth, so that there are no problems in measuring $N(4)$ and $N(5)$. The weakest lines of each J level are often crucial in determining the column density of a given J -level. Only in sightlines where $\log N(J)<15$ do the stronger H_2 lines contain significant column density information. On the other hand, the stronger lines allow one to obtain a reasonable estimate of b , which is set by the maximum equivalent width.

At high column densities ($N(J)>10^{17.5}$ cm⁻²), some or all of the H_2 $J=0-3$ absorption lines develop damping wings. In these cases a Voigt profile was fit to the damping wings, leading to relatively reliable column densities. In the column density range $\log N(J)=15.8-$

16.6, which method was used depends on the implied b -value, and on the ease of fitting a Voigt profile to the strongest lines. The decision is sightline dependent – details can be provided upon request. If there are multiple H_2 components, the procedure outlined above was repeated for each component separately. The selection of lines used may differ, depending on what blending with other lines is present. In many cases no lines of a particular J level are detectable, and only an upper limit can be derived. The numerical value of of this limit is set to the column density corresponding to twice the error on the equivalent width of the strongest unblended line(s), assuming it has an FWHM of 9 km s^{-1} . Two sigma is used because there are always several lines that give similar limits and that thus reinforce each other. This is also obvious from overplotting the theoretical profiles.

4) *Obtaining temperatures.* Given a b -value (see point 5 below), the method described above yields a set of column densities. The ratios of $N(J + 1)$ to $N(J)$ can be described using the Boltzmann distribution:

$$\frac{N(J + 1)}{N(J)} = \frac{g_{J+1}}{g_J} \exp\left(\frac{-(E_{J+1} - E_J)}{kT_{J(J+1)}}\right), \quad (2)$$

with g_J the statistical weights (1, 9, 5, 21, 9, 33 for $J=0, 1, 2, 3, 4, 5$) and E_J the excitation energies of the different levels (0, 0.01469, 0.04394, 0.08747, 0.14491 and 0.21575 eV, respectively) (see Abgrall et al. 1993a). Thus, the five column density ratios $N(1)/N(0)$, $N(2)/N(1)$, $N(3)/N(2)$, $N(4)/N(3)$, and $N(5)/N(4)$ can be converted to five “ratio temperatures”, T_{01} , T_{12} , T_{23} , T_{34} , T_{45} . If the excitation of the H_2 molecule is purely collisional and in equilibrium, these five temperatures will be the same. In reality, T increases for higher level ratios because of radiative excitation. Here, the ratio temperatures are considered purely as way to parametrize the column densities: the (up to) six measured column densities can be parametrized by (up to) six parameters: four ratio temperatures, the total H_2 column density and the intrinsic width.

5) *Deriving b .* At this point the derivation of the preferred value of b can be discussed. There are two methods, which give comparable results when they can both be applied. First, one can do a combined χ^2 fit to the equivalent widths of all lines without damping wings to derive a best-fit b . However, it turns out that this method is not always robust. Sometimes the resulting value for b implies wildly varying ratio temperatures (including $T_{23} < T_{01}$, which is not physical). At high $N(\text{H}_2)$ often just a few $J=4$ or $J=2/3$ lines can be used. At low $N(\text{H}_2)$ most lines are on the linear part of the curve-of-growth and thus the column densities are insensitive to b . The best case happens at intermediate $N(\text{H}_2)$ where reasonable curves-of-growth can be made. However, except for two sightlines (see below) the data are too noisy to provide good constraints on b based on more than two J -levels.

A second method, used for the remainder of this paper, is to assume that $T_{12}=T_{23}$. Then there is only one value of b at which the value of $N(2)$ predicted from T_{12} ($=T_{23}$) and

$N(1)$ is the same as the observed value of $N(2)$, given a value for b . This method is robust, and gives unique solutions. It was invented after the results obtained for temperatures and linewidths using more traditional methods often yielded $T_{12} \sim T_{23}$. Therefore, it was decided to enforce this equality for sightlines where the data do not readily allow one to derive T_{12} and T_{23} independently. It should be noted, however, that the assumption that $T_{12} = T_{23}$ may be incorrect, especially for sightlines through denser disk gas. However, only for sightlines that have high signal-to-noise data combined with intermediate H_2 column density ($\log N \sim 15.3$ to 16.3) is it possible to measure independent b values for several J levels. For the current sample of high-latitude extragalactic targets with $S/N > 10$ *FUSE* data the assumption that $T_{12} = T_{23}$ can be justified by the following considerations.

1) One justification comes from the 30 H_2 components where a combined χ^2 fit to b does yield a useful answer because there are many weak and strong $J=2, 3$ and/or $J=4$ lines. The b -values from the $T_{12} = T_{23}$ method are given in Col. 9 of Table 3, those from a direct fit in Col. 10. The correlation coefficient of $b(\chi^2 \text{ fit})$ vs $b(T_{12} = T_{23})$ is 0.85. The ratio of the two has a distribution with average 1.00 and dispersion 0.10, while their difference is $-0.1 \pm 0.9 \text{ km s}^{-1}$. Note that the typical uncertainty on b is about 2 km s^{-1} . So, in the cases where b could be estimated in two ways the two methods give consistent results.

2) A second justification comes from the two components with good S/N and intermediate-strength H_2 where b can be fitted independently for three J levels: at $+28 \text{ km s}^{-1}$ toward 3C 273.0 and at -44 km s^{-1} toward PG 1116+215. Using the FWHMs and column densities found separately for each J , these yield $T_{01} = 209 \pm 30 \text{ K}$, $T_{12} = 295 \pm 25 \text{ K}$, $T_{23} = 285 \pm 15 \text{ K}$ for 3C 273.0 and $T_{01} = 163 \pm 32 \text{ K}$, $T_{12} = 222 \pm 36 \text{ K}$, $T_{23} = 219 \pm 22 \text{ K}$ for PG 1116+215 K. Compare these to the values in Table 3: $T_{01} = 184 \text{ K}$, $T_{23} = 270 \text{ K}$ for 3C 273.0, and $T_{01} = 167 \text{ K}$, $T_{23} = 219 \text{ K}$ for PG 1116+215. It is clear that T_{12} equals T_{23} to within the errors, but also that it is different from T_{01} .

3) A final justification can be found by trying to make fits assuming that $T_{12} = T_{01}$, rather than $T_{12} = T_{23}$. However, not all sightlines are suitable for this comparison. First, for sightlines with $N(H_2) > 18$, the $J=0$ and $J=1$ lines have damping wings, and thus $N(0)$, $N(1)$ and T_{01} are independent of b . Also, as can be seen from Table 3, T_{01} and T_{23} are rather similar for these sightlines, so T_{12} will be similar to either one. Second, since $N(H_2)$ is more difficult to fit for sightlines with two-component H_2 , these are not suitable for a detailed test. Third, targets with extended UV emission are also unsuitable. Finally, a high S/N ratio is best. There are 15 targets with $S/N > 15$, $\log N(H_2) < 16$, and a single H_2 component: Mrk 279, Mrk 817, PG 1259+593, PKS 2155–303, 3C 273.0, Mrk 421, H 1821+643, HE 0226–4110, PG 0953+414, Mrk 1383, NGC 4670, Ton S210, PKS 0558–504, PKS 0404–12, PKS 2005–489. For all these one combination of $N(H_{2,\text{total}})$, b , T_{01} , T_{23} and $T_{12} = T_{23}$ yields a good parametrization of the observed $N(0)$ to $N(3)$. However, assuming $T_{12} = T_{01}$ always leads to a value for $N(2)$ predicted from $N(1)$ and T_{01} that lies a factor 2 to

3 below the observed value. That means that there is no value for b that gives a combination of $N(0)$ to $N(3)$ for which the ratio $N(1)/N(0)$ implies the same temperature as the ratio $N(2)/N(1)$, but there is a value of b for which the $N(3)/N(2)$ ratio implies a temperature that also fits the ratio $N(2)/N(1)$.

In summary, it is always possible to parametrize the five observed column densities with five observed parameters $\log N(\text{H}_2, \text{total})$, b , T_{01} , and T_{23} , T_{34} , with $T_{12}=T_{23}$. This last assumption was tested in a number of sightlines, and is applied to all sightlines.

Determining the column density is difficult, but obtaining useful errors adds even more complications. There are several sources of uncertainty. The noise in the data and the placement of the continuum allow the calculation of an error for each individual equivalent width measurement. In principle, estimating the continuum placement error requires fitting a separate continuum over a small wavelength range near each absorption line. Since this is impractical because of the large number of targets in the sample, a larger wavelength range was used to fit the continuum across many H_2 lines at once. This results in underestimating the contribution of the continuum placement error to the equivalent width error. However, the targets all have relatively high S/N and mostly flat continua, so the continuum placement error is always small relative to the error associated with the noise itself.

Given a set of equivalent widths and errors, the error in $N(\text{H}_2)$ is found as follows. First the best-fit value of b is used to estimate errors in $N(J)$, using the 68% confidence interval in χ^2 . Then an estimate for the error in b follows from the minimum and maximum value of b for which the fit for $N(\text{H}_2)$, b , T_{01} and T_{23} predicts values for $N(2)$ and $N(3)$ that are still within the 1σ error of those column densities. Next, the errors in $N(J)$ are recalculated, using the implied range of b values.

6) *Theoretical profiles.* Given the derived values for $N(\text{H}_2)$, b , T_{01} , T_{23} , and T_{34} , it becomes possible to create theoretical profiles for the H_2 absorption spectrum. This is done by creating a combined optical depth profile, turning this into an absorption spectrum and then smoothing with the instrumental profile (assumed to be gaussian). These profiles are overplotted on the H_2 lines, and compared to the observed profiles. The whole procedure described in this subsection is then iterated upon until the theoretical profiles look reasonable. In the course of this comparison it was found that the resolution of the *FUSE* LiF (SiC) spectra is indeed ~ 20 (25) km s^{-1} for most observations. However, in two circumstances it was necessary to degrade it to ~ 25 (30) km s^{-1} . This is the case for 27 targets with a single integration longer than 40 ks, and for 5 more targets for which three or more integrations had to be combined. Three targets fall in both categories, while for 8 targets with long exposures the resolution did not appear to be degraded.

A few targets have extended UV emission. Thus, light from different parts of the source is focused on a different part of the detector, effectively increasing the width of the

interstellar absorption lines. In these sightlines it was therefore necessary to smooth the theoretical profiles with broader gaussians in order to properly match the strong and weak lines simultaneously. In a few cases this effect is mild, and a 30 km s^{-1} wide gaussian is needed (Mrk 116, NGC 604, NGC 625, NGC 5253, NGC 7714). In three cases the broadness of the profiles is easily visible in the spectra themselves, and gaussian fits to the H_2 lines yield average widths of 45 km s^{-1} for NGC 1068, NGC 5236 and 80 km s^{-1} for NGC 3310 (see Fig. 2e).

4. Results and Discussion

4.1. Measurements

Table 3 presents the derived H_2 column densities for each J -level, as well as the full-width-half-max (W) and temperatures, separately for the low-, intermediate- and high-velocity gas visible in the 21-cm spectrum. For some components two values of the FWHM are given, in Cols. 9 and 10. The values in Col. 10 are the ones determined from a combined curve-of-growth fit to all H_2 lines, while the values in Col. 9 are determined using the $T_{12}=T_{23}$ assumption. Figure 1 shows the observed and modeled H_2 spectrum over a 9 \AA range for twelve sightlines that span the range of measured H_2 column densities. This part of the spectrum (1047 to 1056 \AA) contains lines of $J=0, 1, 2, 3, 4$ and 5 , as well as two metal lines (Ar I $\lambda 1048,220$, Fe II $\lambda 1055.262$). The figure shows that for $\log N(\text{H}_2) \sim 16.6$ to 18.6 the apparent depth of the L(4-0) R(2) $\lambda 1051.498$, L(4-0) P(2) $\lambda 1053.284$ and L(4-0) R(3) $\lambda 1053.976$ lines barely varies. This is because these lines are all saturated, and their apparent depth is just a reflection of the smoothing with the instrumental profile. For example, for the parameters measured for Mrk 509 ($\log N(\text{H}_2)=17.31$, $\text{FWHM}=10.5 \text{ km s}^{-1}$, $T_{01}=113$, $T_{23}=171$, $T_{34}=254$): $\tau(\lambda 1049.367)=431$, $\tau(\lambda 1049.960)=583$, $\tau(\lambda 1051.033)=273$, $\tau(\lambda 1051.498)=41$, $\tau(\lambda 1053.284)=24$, $\tau(\lambda 1053.976)=8.5$, $\tau(\lambda 1047.550)=0.19$.

In 9 sightlines one, two or three lines of $J=5$ are detected, while toward HS 0624+6907, Mrk 116, and Mrk 1095 five $J=5$ lines can be seen. The implied values for $N(5)$ are listed in the notes, as are the implied values for T_{45} . The ratio of T_{45} to T_{34} is usually between 1.6 to 2.3, but there are not enough well-determined values for T_{45} to study this systematically.

Low-velocity H_2 is detected toward 65 background targets, with column densities ranging from $1 \times 10^{14} \text{ cm}^{-2}$ (NGC 1705) to $6 \times 10^{19} \text{ cm}^{-2}$ (NGC 7469). Upper limits are set in 8 directions. However, H_2 with column density below these upper limits is seen in a few directions, and at least some of the non-detections can be attributed to an insufficiently high S/N ratio. Toward the sightline with the highest $N(\text{H}_2)$ (NGC 7469) weak HD is also detected (see Wakker et al. 2003). HD is not seen in any other sightline.

Intermediate-velocity H_2 is detected in 16 sightlines out of 35 with intermediate-velocity H I. In Sect. 4.4 these detections are compared to the results of Richter et al. (2003), who

studied 61 IVC components in 56 sightlines, many with lower S/N ratio than the sample in this paper. They reported 31 detections. In the current sample, high-velocity H I is found toward 19 sightlines, but only toward NGC 3783 is high-velocity H₂ absorption found, see Sect. 4.2. Finally, H₂ is seen in five external galaxies, as described in Sect. 4.6 below.

4.2. Sightline discussion

In this subsection special sightlines are discussed and comparisons are made with previously published values.

Shull et al. (2000) listed preliminary Milky Way H₂ column densities for four sightlines to AGN. The results for the low-velocity component toward Mrk 876 are not very different: (old vs new) $N=18.36$ vs 18.13 , $\text{FWHM}=5$ vs 7.5 km s⁻¹, $T_{01}=135$ vs 114 K, $T_{23}=200$ vs 163 K, but the intermediate-velocity component was not reported by Shull et al. (2000). For ESO141–G55 there is also generally good agreement, except for T_{23} (19.28 vs 19.29 , 10 vs 6.0 km s⁻¹, 113 vs 97 K, 112 vs 540 K. $N(\text{H}_2)$ increases by a factor 2 toward PG 0804+761 (18.78 vs 19.09 , 8 vs 10.7 km s⁻¹, 113 vs 107 K, 180 vs 119 K), while the limit toward PKS2155–304 was improved from 14.65 to 14.49 .

3C273.0. Sembach et al. (2001b) measured all the intergalactic and interstellar lines in this sightline, including the Galactic H₂. They noticed that the H I and the metal lines do not align with the H₂. A 21-cm spectrum gives $v(\text{H I}, 21\text{-cm})=-6$ and $+25$ km s⁻¹, while the metal lines in the STIS E140M data are at -14 and $+22$ km s⁻¹. Sembach et al. (2001b) argued that $v(\text{H}_2)=+16$ km s⁻¹, and found $\log N(0,1,2,3,4)=15.00\pm 0.30$, 15.48 ± 0.18 , 14.76 ± 0.12 , 14.73 ± 0.12 , and <14.4 , with a FWHM of 10 ± 3 km s⁻¹, implying $T_{01}=157\pm 100$ K. Using the method described in Sect. 2.2, aligning the metal lines in the FUSE data with those in the STIS spectrum implies $v(\text{H}_2)=+28$ km s⁻¹, with $N(0,1,2,3,4)=15.14\pm 0.12$, 15.69 ± 0.11 , 14.90 ± 0.07 , 14.71 ± 0.06 , 13.73 ± 0.12 , $\text{FWHM}=7.2\pm 0.2$ km s⁻¹, and $T_{01}=184$ K. These column densities differ by only about 0.1 dex (<1 σ), and are thus effectively the same. Sembach et al. (2001b) further claimed not to find H₂ absorption associated with the -14 km s⁻¹ metal line component. However, as Fig. 2a shows, a weak secondary H₂ component with $N(\text{H}_2)=14.84$ can clearly be discerned at $v=-9$ km s⁻¹. It is seen in 3 $J=0$, 14 $J=1$, 4 $J=2$ and 7 $J=3$ lines.

Mrk 153. The sightline toward Mrk 153 is extremely unusual, as in addition to the “normal” Galactic H₂ component with $\log N(\text{H}_2)=15.51$ at -20 km s⁻¹ there is also a component with $\log N(\text{H}_2)=16.14$ at a velocity of $+75$ km s⁻¹ ($\text{FWHM}=8.5$ km s⁻¹). This is illustrated in Fig. 2b/d. The dashed lines show the H₂, H I and O I $\lambda 1039.230$ line at -20 km s⁻¹, while the dotted lines indicate the $+75$ km s⁻¹ component.

No H I emission is seen at $+75$ km s⁻¹ in the Leiden-Dwingeloo Survey (LDS) of Hart-

mann & Burton (1997) (36' beam). However, an Effelsberg 21-cm spectrum (9' beam) toward this target shows a weak ($N(\text{H I})=6.4\times 10^{18} \text{ cm}^{-2}$), narrow (FWHM=8.2 km s⁻¹) component at a velocity of +73 km s⁻¹ (Fig. 2d). Note that FWHM(H I)~FWHM(H₂). This may represent a very small cloud or even a circumstellar shell, so that beam dilution reduces the 21-cm brightness temperature to be below the detection limit of the LDS. H I with similar velocities is not detected in any other direction near Mrk 153 ($l=156^\circ.73$, $b=56^\circ.01$). On the other hand, in the HVC catalog of Wakker & van Woerden (1991) small (compact) H I clouds with $v_{\text{LSR}}\sim 80\text{--}110 \text{ km s}^{-1}$ are common at $l>170^\circ$, $b<60^\circ$. It is possible that the object seen toward Mrk 153 is an outlier in this population.

The ratio of the beam areas of the Dwingeloo and Effelsberg telescopes is 16, so a cloud with a diameter of 9' or less that has $T_B=0.4 \text{ K}$ at 9' resolution would have $T_B<0.025 \text{ K}$ in a 36' beam, which is well below the rms noise of the LDS data (0.05 K). Such a cloud might be detectable in an 1' resolution interferometer map, however. If the cloud is smaller than 9' the value of $N(\text{H I})$ derived from the Effelsberg 21-cm brightness temperature scales with the assumed cloud diameter α (in arcmin) as $N(\text{H I})=6.4\times 10^{18} (81/\alpha^2) \text{ cm}^{-2}$.

Using an assumed size α , and defining D_{kpc} as the cloud's distance in kpc (so that its diameter $d=\alpha D_{\text{kpc}}$), the volume density in this cloud is $n_{\text{H}}=N(\text{H I})/d = 577 \alpha^{-3} D_{\text{kpc}}^{-1} \text{ cm}^{-3}$. In formation-dissociation equilibrium, the H₂ and H I volume densities are related by:

$$\frac{n(\text{H}_2)}{n(\text{H I})} = \frac{\langle k \rangle \beta_0}{n_{\text{H}} R} \quad (3)$$

(Spitzer 1978), where $\langle k \rangle=0.11$ is the probability that the H₂ molecule is dissociated after photoabsorption, β_0 is the photoabsorption rate per second, and R is the H₂ formation rate in cm³s⁻¹. Assuming that the formation rate in halo gas is similar to that in disk gas, defining χ as the strength of the interstellar UV radiation field relative to that near the Sun, and defining ϕ as the fraction of the H I gas in the line of sight through the cloud that is physically related to the molecular hydrogen, Richter et al. (2003) turn this equation into:

$$n_{\text{H}} \sim 1.8 \times 10^6 \frac{N(\text{H}_2)}{N(\text{H I})} \frac{\chi}{\phi} \text{ cm}^{-3}. \quad (4)$$

According to the model of the Galactic radiation field presented by Fox et al. (2005), at a latitude of $b=56^\circ$, and for large distances from the Sun, the ionizing radiation field drops as about $\chi\sim 0.03/D_{\text{kpc}}$. Then, $n_{\text{H}}=1.4 \alpha^2 D_{\text{kpc}}^{-1} \phi^{-1} \text{ cm}^{-3}$. Combining all these results yield $\alpha^5=412\phi$. Since $\phi<1$, this means that formation-dissociation equilibrium implies $\alpha<3.3$ arcmin. This in turn would mean $N(\text{H I})>4.8\times 10^{19} \text{ cm}^{-2}$, $n_{\text{H}}<15 D_{\text{kpc}}^{-1} \text{ cm}^{-3}$, and $d=1.1 D_{\text{kpc}} \text{ pc}$.

The +75 km s⁻¹ cloud is also seen in three metal lines. O I $\lambda 1039.230$ has an equivalent width of $65\pm 10 \text{ m}\text{\AA}$, EW(N I $\lambda 1134.980$)= $23\pm 9 \text{ m}\text{\AA}$, and EW(Si II $\lambda 1020.744$)= $43\pm 11 \text{ m}\text{\AA}$. Assuming an intrinsic FWHM of 8.2 km s⁻¹, and using the 21-cm H I measurement (the Ly-

man lines in the FUSE spectrum are too confused) these equivalent widths imply column densities $N(\text{O I}) = 8.2_{-3}^{+18} \times 10^{15} \text{ cm}^{-2}$, $N(\text{N I}) = 6.3_{-3.0}^{+4.2} \times 10^{13} \text{ cm}^{-2}$, $N(\text{Si II}) = 7.2_{-3.7}^{+8.4} \times 10^{14} \text{ cm}^{-2}$. which correspond to abundances $A(\text{O I}) = -0.41 + 2 \log(\alpha/3.3)$, $A(\text{N I}) = -1.80 + 2 \log(\alpha/3.3)$, $A(\text{Si II}) = -0.35 + 2 \log(\alpha/3.3)$. Since α should be < 3.3 arcmin, this implies a subsolar abundance for this cloud. Although there is no strong evidence, a strongly subsolar (< -1) abundance seems unlikely, so α is probably > 1 arcmin. If the H_2 and H I are well-mixed, this cloud may be a low density ($100\text{--}1 \text{ cm}^{-3}$), $0.1\text{--}10$ pc diameter cloud in the Galactic Halo ($D=0.1\text{--}10$ kpc), with slightly subsolar abundances.

Mrk 876. This sightline passes through several especially interesting H I structures, including two HVC complex C components at -173 and -133 km s^{-1} and the Draco Nebula at -30 km s^{-1} . The metal-line absorption associated with the HVC was studied by Murphy et al. (2000), who used the CalFUSE v1.8.7 calibration and only the first observation (P1073101). The head of the Draco Nebula was studied in detail in several papers by Mebold and co-workers (see Mebold et al. 1985, Herbstmeier et al. 1993 and references therein), who argued for a distance of about 1 kpc ($z \sim 0.5$ kpc) for this cloud. There is no H_2 absorption at the velocity of the HVC, down to a limit of $\log N(\text{H}_2) = 14.06$, but the Draco Nebula is clearly detected in H_2 , although it blends with the low-velocity ($v = -2 \text{ km s}^{-1}$) component. Example H_2 lines are shown in Fig. 2c. This is also a case where without very careful alignment of the different segments the intermediate- and low-velocity H_2 would blend too much to measure separately, especially since the first exposure of Mrk 876 is one of the few with a remaining slope in the wavelength scale, and not accounting for this would smear out the IVC H_2 at the edges of the LiF1A and LiF2B segments.

The implied FWHM of the H_2 absorption is 8.8 km s^{-1} , smaller than the 14.7 km s^{-1} seen in the $9'$ resolution Effelsberg H I spectrum. The H I column density in the Effelsberg data is $6.9 \times 10^{19} \text{ cm}^{-2}$. Combining this with $\log N(\text{H}_2) = 15.47$, Eq. 4 implies a density of $77 \chi / \phi$ if the H_2 and H I are in equilibrium. Although the Draco Nebula appears to be relatively close to the plane ($z \sim 500$ pc), it is above much of the dust and thus χ probably lies somewhere between 0.05 and 0.5. Since ϕ is probably ~ 1 in this case, a hydrogen density of $4\text{--}40 \text{ cm}^{-3}$ is implied.

NGC 1068, NGC 3310. These sightlines are special cases in that they need to be smeared with a gaussian having an FWHM of 45 km s^{-1} (NGC 1068) or 80 km s^{-1} (NGC 3310). This is easily justified, however, because both objects have extended ($\sim 30''$) UV emission that basically fills the FUSE LWRS aperture. Toward NGC 1068 the $J=2$ and $J=3$ column densities can still be determined using a curve-of-growth, but a 100 km s^{-1} wide window is needed. In both sightlines the $J=0$ and $J=1$ column densities require Voigt profile fits. Toward NGC 3310 the fitting is rather difficult, as there are two H I clouds in the line of sight – the IV-Arch at -47 km s^{-1} ($N(\text{H I}) = 6.4 \times 10^{19} \text{ cm}^{-2}$), and local gas at -17 km s^{-1} with

$N(\text{H I})=7.7\times 10^{19}\text{ cm}^{-2}$ (see Wakker et al. 2001). Both of these appear to have relatively high $N(\text{H}_2)$: 7.8×10^{18} and $5.4\times 10^{18}\text{ cm}^{-2}$, respectively. Thus, a special method was used to determine $N(J)$. First, a combined curve-of-growth fit was made to the $J=2$ and $J=3$ lines, separately for each component. This yields a b -value. Next the unblended positive- and negative-velocity wings of $J=0$ and $J=1$ lines were fitted to estimate $N(0)$ and $N(1)$ in both components. Then T_{01} was set for the implied $N(\text{H}_2)$, using the $N(\text{H}_2)$ vs T_{01} correlations discussed in Sect. 4.7. Finally, T_{23} and T_{34} were assumed to be equal to T_{01} – without this assumption the theoretical profiles for $J=2$ and $J=3$ lines are too deep. Figure 2e shows some examples of H_2 absorption lines toward NGC 3310. The thick lines show the profiles using an $\text{FWHM}=80\text{ km s}^{-1}$ gaussian. The thin lines show the result that would be obtained with the usual 20 km s^{-1} resolution.

The high H_2 column densities toward NGC 3310 are unusual, but they are implied by the data. A map of the IVC using the LDS data shows that the sightline passes through a rather small ($<1^\circ$) core. It is possible that the extended UV source picks out a tiny piece of the IVC (and also of the low-velocity gas) that does have high $N(\text{H}_2)$. This could be completely accidental, or it could mean that small high-density molecular clouds are common, and will be seen against extended UV sources. A possible way to confirm or deny this would be to obtain several spectra of NGC 3310 with the *FUSE* MDRS or HIRS slit placed at different positions.

NGC 3783. The direction toward NGC 3783 contains a high-velocity cloud at about $+240\text{ km s}^{-1}$, which has been relatively well studied (West et al. 1985; Lu et al. 1994, 1998; Sembach et al. 2001a; Wakker et al. 2002). This HVC (HVC 287+23+240 or WW 187) has metal abundances ~ 0.25 times solar and is interpreted as a core in the Leading Arm of the Magellanic Stream. Sembach et al. (2001a) reported strong H_2 absorption in this cloud, with 30 uncontaminated lines seen. Their analysis produced the following parameters: $\log N(0,1,2,3,4)=16.24\pm 0.20, 16.64\pm 0.10, 15.20\pm 0.08, 14.80\pm 0.08, <14.6$, which corresponds to $\log N(\text{H}_2)=16.80\pm 0.10, T_{01}=133^{+37}_{-21}\text{ K}, T_{23}=241^{20}_{-17}\text{ K}$ and $\text{FWHM}=20\text{ km s}^{-1}$. The analysis presented in this paper yields $\log N(0,1,2,3,4)=17.67\pm 0.70, 18.00\pm 0.70, 16.60\pm 0.50, 15.49\pm 0.20, 14.00\pm 0.13, \log N(\text{H}_2)=18.17, \text{FWHM}=8.2\text{ km s}^{-1}, T_{01}=117\text{ K}, T_{23}=127\text{ K}$.

The main reason for the difference in these column densities is the very different conclusion reached concerning the intrinsic FWHM (20 vs 8.2 km s^{-1}). This seems to be caused by the fact that Sembach et al. (2001a) decided that the weakest $J=2$ and $J=3$ lines (L(2-0) P(2) $\lambda 1081.267$, L(1-0) P(2) $\lambda 1096.438$, L(1-0) R(3) $\lambda 1096.725$, L(1-0) P(3) $\lambda 1099.787$) were not detected, as can be seen from their table of equivalent widths. In Fig. 3 some examples of the profiles implied by the two descriptions are compared. Those implied by the H_2 column densities and FWHM in Table 3 shown as thick solid lines, while the ones implied by the values given by Sembach et al. (2001a) are shown as thin solid lines. Clearly, for $J=0, J=1$ and for strong $J=2$ and $J=3$ lines, the two prescriptions produce almost the same result.

There are some subtle differences in detail, such as near $v_{\text{LSR}}=190 \text{ km s}^{-1}$ in the W(0-0) Q(1) $\lambda 1009.771$ and L(4-0) P(1) $\lambda 1051.033$ panels, both showing that the thick lines give a slightly better prediction. The main difference is that the low- b , high- N profile is clearly much better for the L(1-0) R(2) $\lambda 1094.244$, L(1-0) P(2) $\lambda 1096.438$, L(1-0) R(3) $\lambda 1096.725$, and L(1-0) P(3) $\lambda 1099.787$ lines. The second and third of these four mix with the low-, intermediate- and high-velocity Fe II lines, but by comparing the profile with other Fe II lines it is clear that the high-velocity H_2 lines are not blended with Fe II.

It should be noted that the Sembach et al. (2001a) analysis was based on just the first 37 ks exposure of this object, whereas the current analysis uses all seven exposures (totaling 196 ks). However, even in the first exposure the weakest $J=2$ and $J=3$ absorption lines clearly show the high-velocity component.

This comparison provides a prime illustration of how difficult it is to determine H_2 column densities in the range $\log N(\text{H}_2)=16.5$ to 18.2. For strong lines there is little difference in a low- b , high- N vs a high- b , low- N profile, since the lines have not yet developed damping wings. Only the weakest $J=2/3$ lines contain some information that allows one to constrain b , and the final result is rather sensitive to those weak lines.

Wakker et al. (2002) found that the H I column density in the HVC toward NGC 3783 is $8.3 \times 10^{19} \text{ cm}^{-2}$, implying a molecular fraction $f(\text{H}_2)=2 N(\text{H}_2)/(2 N(\text{H}_2)+N(\text{H I}))$ of 0.03. Since this cloud is likely to be part of the Leading Arm of the Magellanic Stream, at a distance of 50 to 100 kpc, the hydrogen volume density implied by Eq. 4 is $\sim 10 (D/100 \text{ kpc}) \phi^{-1}$. This can be compared to the volume densities of 20 cm^{-3} implied by the high-resolution ($1'$) H I data. The high-resolution H I maps of Wakker et al. (2002) show that NGC 3783 does not lie in the direction of a bright subcore in the HVC, so the fact that there still is a substantial amount of H_2 suggests that ϕ is large. Thus, it appears likely that the H_2 and H I in this cloud are in formation-dissociation equilibrium, contrary to the conclusion of Sembach et al. (2001a).

4.3. Molecular fraction

Figure 4 a presents a plot of the average molecular fraction in each sightline, defined as

$$f(\text{H}_2) = \frac{2 N(\text{H}_2)}{2 N(\text{H}_2) + N(\text{H I})}. \quad (5)$$

Solid points are for low-velocity gas, i.e. only H I and H_2 components at absolute velocities less than 30 km s^{-1} were used. Open points are for the intermediate-velocity clouds (see also next subsection).

It should be stressed strongly that for the low-velocity gas these $f(\text{H}_2)$ values have no direct physical meaning. It is almost guaranteed that each sightline contains several gas

clouds with similar velocity, containing both H I and H₂. At the available spectral resolution (and also considering the intrinsic linewidths), the H₂ absorptions of these clouds cannot be separated. Only the total can be measured. Each of this unknown number of clouds contributes an unknown fraction of the H I and H₂ to the total column density that is observed. Any attempt to compare $N(\text{H I})$ and $N(\text{H}_2)$ directly and derive the local fraction of nuclei that is in the form of H₂ will run afoul of this fact. Thus, the usual study of how the molecular fraction varies with H I column density (e.g. Savage et al. 1977) can not be done for the sightlines in the *FUSE* extragalactic sample. Such a study is justified for sightlines to nearby disk stars, where the sightline intersects just one ISM cloud. What can be done is to study how important the H₂ is as a major constituent of the local ISM.

The $f(\text{H}_2)$ vs $N(\text{H I})$ plot shows three regions. a) The four sightlines with $\log N(\text{H}) > 20.75$ are ESO 141–G55, HS 0624+6907, Mrk 1095 and NGC 3783, and they represent four of the nine sightlines at latitudes below 27°. It is interesting that no small values of $f(\text{H}_2)$ are found at high hydrogen column densities, suggesting that at least one of the clouds in the sightline is dense enough have a high molecular fraction.

b) At $\log N(\text{H}) < 20.2$ the average molecular fraction mostly lies between $10^{-3.3}$ and $10^{-5.8}$. The majority of these points correspond to intermediate-velocity clouds (open circles). In this case the comparison *is* physically meaningful, and it implies that $\log N(\text{H})$ has to be larger than ~ 20.2 before a transition to H₂ takes place. The two unusual points at (19.9, –0.9) are for NGC 3310 (where $N(\text{H}_2)$ is very difficult to determine), and for PG 1351+640.

c) In the intermediate region ($\log N(\text{H}) = 20.2$ to 20.7) a large range is seen for $f(\text{H}_2)$. It is likely that for sightlines with low $f(\text{H}_2)$ the H I column density is spread over several clouds, while for sightlines with high $f(\text{H}_2)$ most of the H I column density is concentrated in one high column component.

4.4. IVCs

Table 4 lists the H₂ parameters found for intermediate-velocity gas, both in this paper and in Richter et al. (2003). This shows that similar answers are obtained for 6 of the 18 sightlines (3C 273.0, Mrk 59, Mrk 509, Mrk 876, PG 1259+593, PG 1351+640). In four sightlines (Mrk 279, Mrk 421, Mrk 1513, NGC 7714) the IVC only popped up in the additional data that was obtained after May 2002, i.e. data not included by Richter et al. (2003). In two sightlines (Mrk 817 and NGC 3783) the analysis presented here revealed an IVC component that was not found by Richter et al. (2003). The -45 km s^{-1} component toward NGC 3783 is not seen in H I, although it appears needed to fit some of the stronger H₂ lines. Still, the reality of this component remains in some doubt. New IVC components are found toward three sightlines not included in the Richter et al. (2003) sample: Mrk 153 (see above), NGC 4051 and 1H 0717+714.

Results that differ substantially from those listed by Richter et al. (2003) are found for three sightlines – NGC 3310, NGC 4151 and PG 1116+215. The difficulties with NGC 3310 were described above. Toward NGC 4151 the H I spectrum is complex, with narrow peaks at -41 and -21 km s^{-1} on top of a broad base (see Wakker et al. 2003). A very good H_2 fit can be obtained with a single component at -21 km s^{-1} . Richter et al. (2003) identified this H_2 as associated with the broad IV-Arch component at -29 km s^{-1} . Finally, the PG 1116+215 sightline is noteworthy for the fact that it is the only sightline toward which the intermediate-velocity H_2 is much stronger than the low-velocity H_2 . The FWHM found by Richter et al. (2003) is twice as large as the value found here (13.2 vs 6.5 km s^{-1}). This results in column densities of 15.27 vs 16.01 , respectively. The higher- b , lower- N combination yields similar theoretical profiles for strong lines, but clearly underpredicts the 3 to 5 weakest lines of each J level, as illustrated by Figs. 2g and h. This is not the case for the lower- b , higher- N combination, which must therefore be preferred.

Molecular hydrogen is not seen in all IVCs. Richter et al. (2003) studied a total of 61 IVC components in 56 sightlines, and report 14 clear and 17 tentative detections. Their sample included many sightlines with much lower S/N ratio than the limit in this paper. Figure 4b presents a scatter plot of $\log N(\text{H I})$ vs $\log N(\text{H}_2)$ in the 35 IVCs in the current sample. H_2 is not detected for $N(\text{H I}) < 19.2$, but is seen in 8 of 20 cases (40%) with $N(\text{H I})$ between 19.25 and 19.75, and in 6 of 9 (66%) with $N(\text{H I}) > 19.75$. Thus, the fraction of sightlines with intermediate-velocity H_2 appears to increase with $N(\text{H I})$.

The IVCs in which H_2 is detected include six sightlines through the IV Arch, two through the LLIV Arch, as well as five smaller IVCs. As previously argued by Richter et al. (2003), the fact that H_2 is seen in many IVCs strongly suggests the presence of dust in these clouds.

4.5. HVCs

Richter et al. (2001) studied high-velocity H_2 in two sightlines – Fairall 9 through the Magellanic Stream and PG 1259+593 through complex C. Although these two sightlines have comparable amounts of H I, H_2 was seen toward Fairall 9 $\log N(\text{H}_2) = 16.4$, but not toward PG 1259+593 ($\log N(\text{H}_2) < 13.96$). This led Richter et al. (2001) to conclude that there is dust in the Magellanic Stream but not in complex C, which is supported by the abundance ratios of depleted to undepleted elements in these two objects. That conclusion was further supported by the detection of H_2 toward NGC 3783 reported by Sembach et al. (2001a).

The high S/N sample of this paper does not include Fairall 9, but there are 20 sightlines where high-velocity H I is seen. The only high-velocity H_2 seen remains that toward NGC 3783. Nine of the remaining 19 sightlines pass through complex C, two through complex A, two through the Outer Arm, three through positive-velocity HVCs, two through the trailing part of the Magellanic Stream and one through a compact HVC. Figure 4c shows the

upper limits versus the H I column density, with open squares for the complex C sightlines, open triangles for the other HVCs. Although seven of the nine HVCs have H I column densities >19.25 , i.e. comparable to those seen in the IVCs, no H_2 is seen in complex C down to limits of $\log N(\text{H}_2) < 13.84$. The H I column densities toward the other HVCs are generally lower. Six of the ten have $\log N(\text{H I}) < 19.25$, and by analogy with the IVCs H_2 might not be expected. However, none of the four with higher $N(\text{H I})$ show H_2 either. The implication is that HVCs seem to have little to no dust.

4.6. H_2 in external galaxies

There are five detections of H_2 in external galaxies. These are summarized in Table 4 and described below. Figure 5 shows the wavelength region between rest wavelengths of 1047.7 and 1060.5 Å, but displayed such that the redshifted H_2 lines of the five targets are aligned. The dotted lines and labels indicate the positions of the redshifted metal and H_2 lines, while the dashed lines without labels show the positions of the Milky Way lines. The horizontal bar on the lower left side indicates the velocity of the external galaxy; it shows how far apart each pair of Galactic and extragalactic lines is.

Four of the five H_2 extragalactic detections are in nearby galaxies, with the light provided by hot stars in H II regions. In all cases the H_2 lines are weak, and they are probably associated with the diffuse ISM in front of the H II regions. As the light that is seen is the combined light from many OB stars, both the absorption and the emission spectrum are a combination of many sightlines, and the H_2 absorption is just an average over these. Furthermore, sightlines with low extinction (and thus low $N(\text{H}_2)$) are detected preferentially, so the H_2 column densities are not expected to be representative of the dense ISM in those external galaxies. The H_2 lines also are likely to have substructure, but the S/N ratios and complicated continua of the spectra do not allow a detailed study. Nevertheless, in the end it is possible to proceed as-if the lines originate in a single cloud and derive column densities and temperatures. These turn out to fit the same patterns as the H_2 lines seen in the Milky Way (see Sect. 4.7). However, the resulting column densities should not be thought of as physically meaningful, but as “pseudo column densities” that parametrize the absorption spectrum.

The five extragalactic H_2 detections are now described in more detail, with Mrk 205 being the only case where the background light is not provided by the absorbing galaxy.

Mrk 205. It is well known that the sightline to Mrk 205 intersects the disk of the nearby galaxy NGC 4319 (Bowen et al. 1991, 1995; Bowen & Blades 1993). The sightline passes just 6 kpc from the center of NGC 4319 ($v_{\text{sys}}=1357 \text{ km s}^{-1}$). Only a few other such coincidences between a FUV-bright AGN and a galaxy are known (Ton 1480 passes 7 kpc from NGC 4203, but Ton 1480 is only half as bright as Mrk 205 in the FUV; 3C 232 is even

fainter and passes 13 kpc from NGC 3067 – Keeney et al. 2005). H₂ associated with the disk of NGC 4319 is clearly detected at a velocity of 1281 km s⁻¹. Figure 5a shows several Galactic $J=0, 1, 2$ and 3 H₂ lines, as well as these same lines redshifted by 1281 km s⁻¹. For the fitting care was taken to exclude H₂ lines for which the Galactic component at -5 km s⁻¹ and the NGC 4319 component blend. The parameters for the H₂ in NGC 4319 are $\log N(\text{H}_2)=15.78\pm 0.24$, $T_{01}=271$ K and $T_{23}=353$ K. The expected temperatures for Galactic H₂ (see Sect. 4.7) at this column density are $T_{01}=177$ K and $T_{23}=281$ K. This corresponds to measured values of $N(2)$ and $N(3)$ that are about 0.1 and 0.25 dex higher and $N(0)$ 0.16 dex lower than expected from $N(1)$. These differences are not large and thus it is safe to conclude that the properties of the H₂ in NGC 4319 are similar to those in the Milky Way.

NGC 604. Bluhm et al. (2003) measured the H₂ for several sightlines toward H II regions in M33. One of these (NGC 604) falls in the high S/N sample of this paper. For this sightline, Bluhm et al. (2003) used the A0860101 dataset, which was obtained through the LWRS aperture; they derived upper limits of $\log N(0,1,2,3) < 13.7, < 14.3, < 14.4, < 14.0$. After that paper was published NGC 604 was observed again, but this time through the MDRS aperture (observation B0180201). Although the flux in the new dataset is lower (10.6 vs 31.2×10^{-14} erg cm⁻² s⁻¹ Å⁻¹) as is the S/N ratio (14.1 vs 17.4 at 1063 Å), the H II region is an extended source, so the narrower aperture results in much sharper lines. As a result, one $J=0$, three $J=1$, one $J=2$ and three $J=3$ M33 H₂ lines are detected at the 2 to 6σ level, resulting in approximate column densities of $\log N(0,1,2,3) = 14.3, 14.8, 14.3, 14.5$. Figure 5b shows several of these weak lines. To reconcile the column densities implied by the equivalent widths with the shape of the profiles, it is necessary to assume that the instrumental resolution is 30 km s⁻¹. This is most likely a result of the fact that NGC 604 is an extended source, which smears out the image on the detector. Also, T_{23} is unusually high considering the value of $N(\text{H}_2)$ (see Sect. 4.7), which may be related to the fact that the H₂ absorption is an average between many sightlines.

NGC 625. The data for NGC 625 ($v_{\text{gal}}=396$ km s⁻¹) have a comparatively low S/N ratio (12.1), and the H₂ that may be seen at a velocity of 396 km s⁻¹ is weak, showing 3 to 8σ detections in several $J=0, J=1$ and $J=3$ lines (see Fig. 5c for a few examples). It is clear that these detections are real, even though many lines are a bit ragged around the edges – that is, they seem to show a little broader absorption. There is no clear pattern to this, however, in that lines of the same J level show different substructure. Some of this is probably due to the low S/N ratio, some to stellar lines in some of the stars that provide the light.

NGC 5236 (M 83) and NGC 5253. The detections of extragalactic H₂ at $v=500$ km s⁻¹ in the spectrum of NGC 5236 (M 83) and $v=404$ km s⁻¹ in NGC 5253 were first reported by Hoopes et al. (2004). The continua of these objects have many undulations, caused by

stellar lines, so that the piecewise continuum fit requires many small pieces, leaving some H₂ lines too confused. This also means that the equivalent widths have large systematic errors. These are not taken into account in the fitting process, but it means that the real errors on $N(J)$ are much larger than the quoted values. Figures 5d and e show examples of detected lines. Panel d clearly shows the undulating continuum toward NGC 5236, and shows some artifacts associated with the piecewise fit (e.g. near 1055.5 Å).

For NGC 5236 Hoopes et al. (2004) report only one 1.7σ (25.6 ± 15 mÅ) detection in the L(9-0) R(1) $\lambda 993.018$ line. However, a detailed assessment, and using the carefully aligned and combined LiF1A+LiF2B spectra shows that five $J=0$, nine $J=1$, four $J=2$ and five $J=3$ lines can be seen, with typical equivalent widths of 30 mÅ ($J=0, 2, 3$) or 50 mÅ ($J=1$) and typical errors of ~ 6 mÅ. The FWHM appears to be 12 km s^{-1} , and the implied column density is $N(\text{H}_2) = 1.9 \times 10^{15} \text{ cm}^{-2}$. Compare this to the values of 25 km s^{-1} and $1.8 \times 10^{15} \text{ cm}^{-2}$ listed by Hoopes et al. (2004).

Hoopes et al. (2004) report a few $J=1$ and $J=2$ detections in the spectrum of NGC 5253. In the combined LiF1A+LiF2B spectra used here, two unblended lines of $J=0$, four of $J=1$, 2, and nine of $J=3$ are clearly seen, as are many more blended lines. Detections range from 20 to 70 mÅ, with typical errors of 7 mÅ. The implied column density is $1.7 \times 10^{15} \text{ cm}^{-2}$, with an FWHM of 10 km s^{-1} . Hoopes et al. (2004) listed $2.2 \times 10^{15} \text{ cm}^{-2}$.

In both galaxies, the theoretical profiles constructed using the column densities and the FWHM implied by the curve-of-growth need to be smoothed with a 45 km s^{-1} (NGC 5236) or 30 km s^{-1} (NGC 5253) wide instrumental profile to make them look similar to the observed profiles. This can be explained by the fact that the background galaxies are extended sources. For the same reason, the derived temperatures must represent a mixture of gas in the many sightlines to individual stars. Yet, the average seems to follow the usual $N(\text{H}_2)$ vs T_{01} and T_{23} correlations described in Sect. 4.7.

Toward NGC 5236 the Milky Way molecular hydrogen requires special treatment. It has low column density ($\log N(\text{H}_2) \sim 14.8$). No $J=0$ or $J=2$ lines are detected, but six $J=1$ lines and four $J=3$ lines show up. Assuming the expected T_{01} and T_{23} for $\log N(\text{H}_2) = 14.8$ (see Sect. 4.7) shows that the column densities for these two levels are normal, and that the $J=0$ and $J=2$ should indeed be undetectable at the target's S/N level. Thus, the temperatures listed in Table 3 are the ones expected from the correlations.

4.7. Correlations

Figure 6 shows scatter plots of many combinations of the measured H₂ parameters. Filled circles are for the most reliable measurements, using sightlines with S/N ratio > 13 near 1031 Å (or 1063 Å). Fits to components in sightlines with lower S/N ratio or fits that seemed less reliable for one reason or another are shown as open circles. Clear correlations

exist between the H_2 parameters. Least-squares fits were made to three of the scatter plots, using only the filled circles, giving:

$$T_{01} = -23.7 (\log N(H_2) - 14) + 219 \quad (6)$$

$$\log \frac{N(2)}{N(0)} = -0.323 (\log N(H_2) - 14) + 0.274 \quad (7)$$

$$\log \frac{N(3)}{N(1)} = -0.513 (\log N(H_2) - 14) - 0.046 \quad (8)$$

$$\log \frac{N(4)}{N(3)} = -0.210 (\log N(H_2) - 14) - 0.669. \quad (9)$$

$$(10)$$

These four fits are shown by the solid black lines in panels d, j, l and o of Fig. 6. Using these relations, it is possible to predict values for $N(J)$ given a value for $N(H_2)$. The implied relations for the other panels are shown by the dashed lines. These show that unlike the T_{01} correlation, the correlations between $N(H_2)$ and T_{23} or T_{34} are not linear.

In the dense ISM the quantity T_{01} is likely to be similar to the kinetic temperature of the gas, as proton-exchange collisions are the dominant excitation mechanism. For sightlines with $N(H_2) > 10^{18} \text{ cm}^{-2}$, $\langle T_{01} \rangle = 103 \pm 19 \text{ K}$. This can be compared to the average for the nearby Galactic Disk found by Savage et al. (1977) ($\langle T_{01} \rangle = 77 \pm 17 \text{ K}$), and the average for the LMC disk found by Tumlinson et al. (2002) ($82 \pm 21 \text{ K}$). Clearly, even for the denser high-latitude ISM, $\langle T_{01} \rangle$ is higher than in the Disk. A possible explanation is that the average density of gas sampled by the high-latitude sightlines is lower, and the excitation of the $J=1$ level is no longer purely thermal.

An important conclusion to take away from the correlation between T_{01} and $\log N(H_2)$ is that it is important to specify the H_2 column density range when calculating a value for $\langle T_{01} \rangle$. The fit predicts a value of $T_{01} = 81$ at $\log N(H_2) = 20$, comparable to the high-column density average found by Savage et al. (1977). But at $\log N(H_2) = 15$ the expected T_{01} is 195 K, significantly higher. A hint of this effect was already found by Spitzer & Cochran (1973) in their sample of sightlines through nearby dense disk gas.

Theoretical models of the population level distribution of H_2 were presented by Browning et al. (2002). They take into account the formation of H_2 on dust grains, and the manner in which the higher rotational levels of H_2 are excited by UV radiation. Results for several models are presented, using a standard Galactic radiation field ($\chi=1$), a much stronger field ($\chi=50$), a standard formation rate, and 1/10th the standard formation rate. These results are only expressed in the form of plots of $N(H_2)$ vs $\log N(4)/N(2)$. The few model points that can be obtained from the Browning et al. (2002) paper are overplotted as crosses on panel n of Fig. 6. This shows that the models a) predict values for $N(4)/N(2)$ that are in the correct range at low $N(H_2)$ and b) predict an increase in this ratio as function of $N(H_2)$.

However, the models tend to overpredict $N(4)$ by a factor ~ 10 to 100 at the highest H_2 column densities, and by a factor ~ 50 at $\log N(H_2)=18$.

4.8. Sky map

The distribution of the H_2 column densities on the sky is shown in Figs. 7 and 8. In this representation, each position on the sky is given a color that depends on the value of $N(H_2)$ toward the nearest background target, up to 12 degrees away. Figure 7 is for the northern Galactic sky, Fig. 8 for the southern sky. If an upper limit is found, the area around the background source is only colored out to a radius of 3° . Only H_2 components with $|v_{LSR}| < 25 \text{ km s}^{-1}$ are included in these figures. In the northern sky, $N(H_2)$ is low (< 16.6) for most latitudes above about 45° , the exception being the sightline toward PG 1211+143. In the southern sky the sightlines with higher $N(H_2)$ concentrate around $l=90^\circ$, and there does not seem to be a strong gradient with latitude. In all these sightlines H_2 is a trace constituent of the ISM, as $N(H\text{ I})$ is $> 8 \times 10^{19} \text{ cm}^{-2}$ everywhere.

5. Conclusions

This paper presents measurements of H_2 column densities toward 73 extragalactic targets observed with *FUSE* for which the final combined spectrum has signal-to-noise ratio > 10 . The individual observations were calibrated with the CalFUSE calibration pipeline version 2.1 or 2.4. Final shifts were found for each detector segment, in order to align the metal and H_2 lines with either a 21-cm H I spectrum or a UV spectrum taken with the *STIS* E140M grating on *HST*. H_2 column densities or column density limits were then measured for the low-, intermediate- and high-velocity H I in each sightlines, for each rotational level $J=0$ to $J=4$. For weaker H_2 lines ($N(J) < 16.5$) a curve-of-growth was used to estimate b and N , while Voigt profiles were fit at larger column densities.

These determinations give the following conclusions:

(1) H_2 is seen in almost all (65 out of 73) sightlines toward high-latitude ($|b| > 20^\circ$) extragalactic targets.

(2) In the northern galactic hemisphere $N(H_2)$ is generally below 10^{17} cm^{-2} at latitudes above 45° . In the southern hemisphere $N(H_2)$ shown no correlation with latitude, but instead is higher for $l=40$ to 150° .

(3) There are strong correlations between $N(H_2)$ and the level population ratios, with the average value of T_{01} ranging from 81 K at $\log N(H_2)=20$ to 219 K at $\log N(H_2)=14$.

(4) As is theoretically expected, the level populations of the higher rotational states show a relative increase at lower H_2 column densities, with T_{23} and T_{34} rising to 375 K and 575 K at $\log N(H_2)=15$.

(5) An unusual cloud is seen at a velocity of $+75 \text{ km s}^{-1}$ toward Mrk 153. This cloud has narrow lines ($\text{FWHM} \sim 8.5 \text{ km s}^{-1}$), and must be small, as it is detected in a $9'$ 21-cm beam, but not in a $36'$ beam. It is detected in O I, N I, and Si II lines. It may be a circumstellar shell, or it may be a low density ($100\text{--}1 \text{ cm}^{-3}$), $0.1\text{--}10 \text{ pc}$ diameter cloud in the Galactic Halo ($D=0.1\text{--}10 \text{ kpc}$) with subsolar abundances.

(6) The high-velocity H_2 absorption toward NGC 3783 that was reported by Sembach et al. (2001a) is shown to have an H_2 column density of 18.17, rather than 16.80, because the derived FWHM is 8.2 km s^{-1} , rather than the 20 km s^{-1} reported by Sembach et al. (2001a). This factor 25 difference in column densities only leads to noticeable differences in the H_2 absorption profiles for the weakest $J=2$ and $J=3$ lines, which were reported as non-detections by Sembach et al. (2001a). The implication of the higher value for $N(\text{H}_2)$ is that the H_2 in the HVC may be in formation-dissociation equilibrium with H I after all, rather than being remnant H_2 formed before the tidal interaction.

(7) A comparison of the H_2 in IVCs with the results of Richter et al. (2003) shows that in all but three cases similar results are found. Nine new detections of intermediate-velocity H_2 are reported here.

(8) Intermediate-velocity H_2 is detected in about half of the cases where intermediate-velocity H I is seen, with the fraction increasing toward higher $N(\text{H I})$.

(9) Except for one sightline through the Magellanic Stream (NGC 3783) high-velocity H_2 is not detected in the 19 high-velocity H I clouds intersected by the 73 sightlines, indicating there is little or no dust in HVCs.

(10) Molecular hydrogen is seen in the disks of five external galaxies: NGC 4319, M 33, NGC 625, NGC 5236 (=M 83), and NGC 5253. The detection in NGC 4319 is at a distance of 7 kpc from the center of that galaxy, using the Seyfert Mrk 205 as a background target, giving $\log N(\text{H}_2)=15.783$, and relatively normal Boltzmann temperatures. In the other four cases the detection is the average of many sightlines against OB stars with relatively low extinction, so the low values of $N(\text{H}_2)$ are not representative of the ISM in those galaxies.

I thank Marilyn Meade for (re)calibrating the many *FUSE* datasets. This work was supported by NASA grants NAG5-9179 (LTSA), NNG04GD85G (ADP), NAG5-13687 (*FUSE*) and NNG04GA39G (*FUSE*).

REFERENCES

- Abgrall H., Roueff E., Launay F., Roncin J.-Y., Subtil J.-L., 1993a, *A&AS*, 101, 273
 Abgrall H., Roueff E., Launay F., Roncin J.-Y., Subtil J.-L., 1993b, *A&AS*, 101, 323
 Arnal E.M., Bajaja E., Larrarte J.J., Morras R., Pöppel W.G.L., 2000, *A&ApS*, 142, 35
 Bluhm H., de Boer K.S., Marggraf O., Richter P., Wakker B.P., 2003, *A&A*, 398, 983

- Bowen D.V., Pettini M., Penston M.V., Blades J.C., 1991, MNRAS, 248, 153
- Bowen D.V., Blades J.C., 1993, ApJ 403, L55
- Bowen D.V., Blades J.C., Pettini M., 1995, ApJ 448, 634
- Browning M.K., Tumlinson J., Shull M.J., 2003, ApJ, 582, 810
- Federman, S.R., Glassgold, A.E., Kwan, J., 1979, ApJ, 227, 466
- Fox A.J., Wakker B.P., Savage B.D., Tripp T.M., Sembach K.R., Bland-Hawthorn J., 2005, ApJ, in press
- Gry C., Boulanger F., Nehmé, C, Pineau des Forêts, Habart E., Falgarone E., 2002, A&A, 391, 675
- Hartmann D., Burton W.B., 1997, “Atlas of Galactic Neutral Hydrogen”, Cambridge University Press (LDS)
- Herbstmeier U., Heithausen A., Mebold U., 1993, A&A, 272, 514
- Hollenbach D., Werner M.W., Salpeter E.E., 1971, ApJ, 163, 155
- Hoopes C.G., Sembach K.R., Heckman T.M., Meurer G.R., Aloisi A., Calzetti D., Leitherer C., Martin C.L., 2004, ApJ, 612, 825
- Jenkins E.B., Joseph C.L., Long D., et al., 1988, Proc. SPIE, 932, p213
- Jura M., 1975a, ApJ, 197, 575
- Jura M., 1975b, ApJ, 197, 581
- Keeney B.A., Momjian E., Stocke J.T., Carilli C.L., Tumlinson J., 2005, ApJ, 622, 267
- Krämer G., Barnstedt J., Eberhard N., et al., 1990, in IAU Coll. 123, “Observatories in Earth Orbit and beyond”, eds. Y. Kondo, Kluwer Dordrecht, p177
- Lacour S., Ziskin V., Hébrard G., Oliveira C., Andréé M.K., Ferlet R., Vidal-Madjar A., 2005, ApJ, 627, 251
- Lu L., Savage B.D., Sembach K.R., 1994, ApJ 426, 563
- Lu L., Savage B.D., Sembach K.R., Wakker B.P., Sargent W.L.W. Oosterloo T.A., 1998, AJ, 115, 162
- Mebold U., Cernicharo J., Velden L., Reif K., Crezelius C., Goerigk W., 1985, A&A, 151, 427
- Moos H.W., et al., 2000, ApJ, 538, L1
- Murphy E.M., Sembach K.R., Gibson B.K., Shull J.M., Savage B.D., Roth K.C., Moos H.W., Green J.C., York D.G., Wakker B.P. 2000, ApJ, 538, L35
- Rachford B.L., Snow T.P., Tumlinson J., Shull J.M., Blair W.P., et al., 2002, ApJ, 577, 221
- Richter P., Sembach K.R., Wakker B.P., Savage B.D., 2001, ApJ, 562, L181
- Richter P., Wakker B.P., Savage B.D., Sembach K.R., 2003, ApJ, 586, 230
- Sahnou D.J., et al. 2000, ApJ, 538, L7
- Savage B.D., Bohlin R.C., Drake J.F., Budich W., 1977, ApJ, 217, 291
- Sembach K.R., Savage B.D., 1992, ApJS 83, 147
- Sembach K.R., Howk J.C., Savage B.D., Shull J.M., 2001a, AJ, 121, 992

- Sembach K.R., Howk J.C., Savage B.D., Shull J.M., Oegerle W.R., 2001b, *ApJ*, 561, 573
- Shull J.M., Beckwith S.V.W., 1982, *ARA&A*, 20, 163
- Shull J.M., Tumlinson J., Jenkins E.B., Moos H.W., Rachford B.L., Savage B.D., et al. 2000, *ApJ*, 538, L73
- Spitzer L., Cochran W.D., 1973, *ApJ*, 186, L23
- Spitzer L., Cochran W.D., Hirshfeld A., 1974, *ApJS*, 266, 373
- Spitzer L., 1978, “Physical Processes in the Interstellar Medium (New York, Wiley)
- Spitzer L., Zweibel E.G., 1974, *ApJ*, 191, L127
- Spitzer L., Jenkins E.B., 1975, *ARA&A*, 13, 133
- Tripp T.M., Jenkins E.B., Bowen D.V., Prochaska J.X., Aracil B., Ganguly R., 2005, *ApJ*, 619, 714
- Tumlinson J., Shull J.M., Rachford B.L., Browning M.K., Snow T.P., et al., 2002, *ApJ*, 566, 857
- Wakker B.P., van Woerden H., 1991, *A&A*, 250, 509
- Wakker B.P., Kalberla P.M.W., van Woerden H., de Boer K.S., Putman M.E., 2001, *ApJS*, 136, 537
- Wakker, B.P., Oosterloo, T.A., Putman, M.E., 2002, *AJ*, 123, 1953
- Wakker B.P., Sembach K.R., Savage B.D., Richter P., Meade M., et al., 2003, *ApJS*, 146, 1
- West K.A., Pettini M., Penston M.V., Blades J.C., Morton D.C., 1985, *MNRAS*, 215, 481

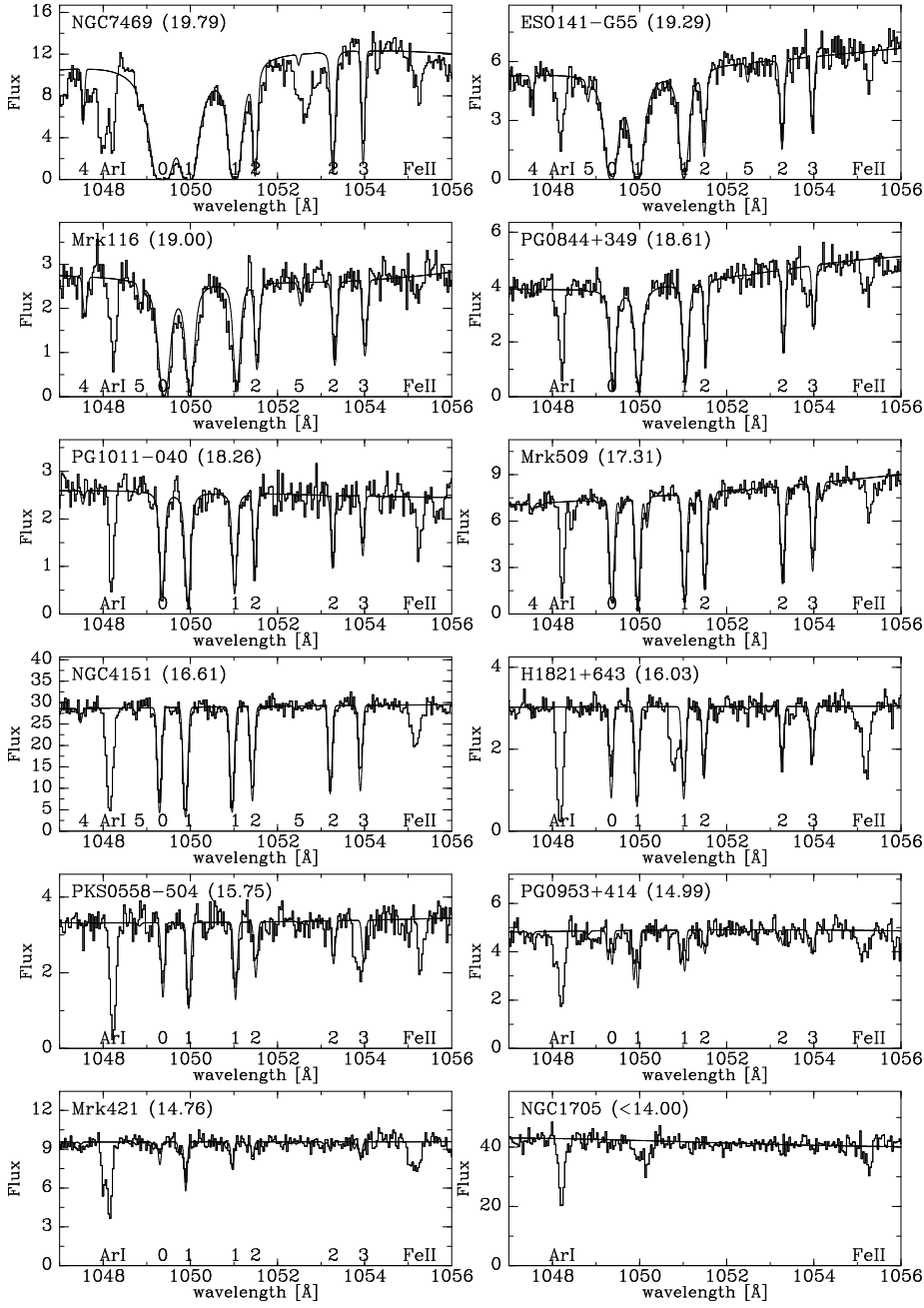


Fig. 1.— Part of the spectrum for 12 sightlines representative for the range of observed H₂ column densities. This 9 Å range contains lines of $J=0, 1, 2, 3,$ and $4,$ whose wavelengths are shown by the numerical labels along the bottom axes. Overplotted on the data are theoretical profiles calculated using the H₂ parameters listed in Table 3. The number in parentheses after the name of each target gives $\log N(\text{H}_2)$.

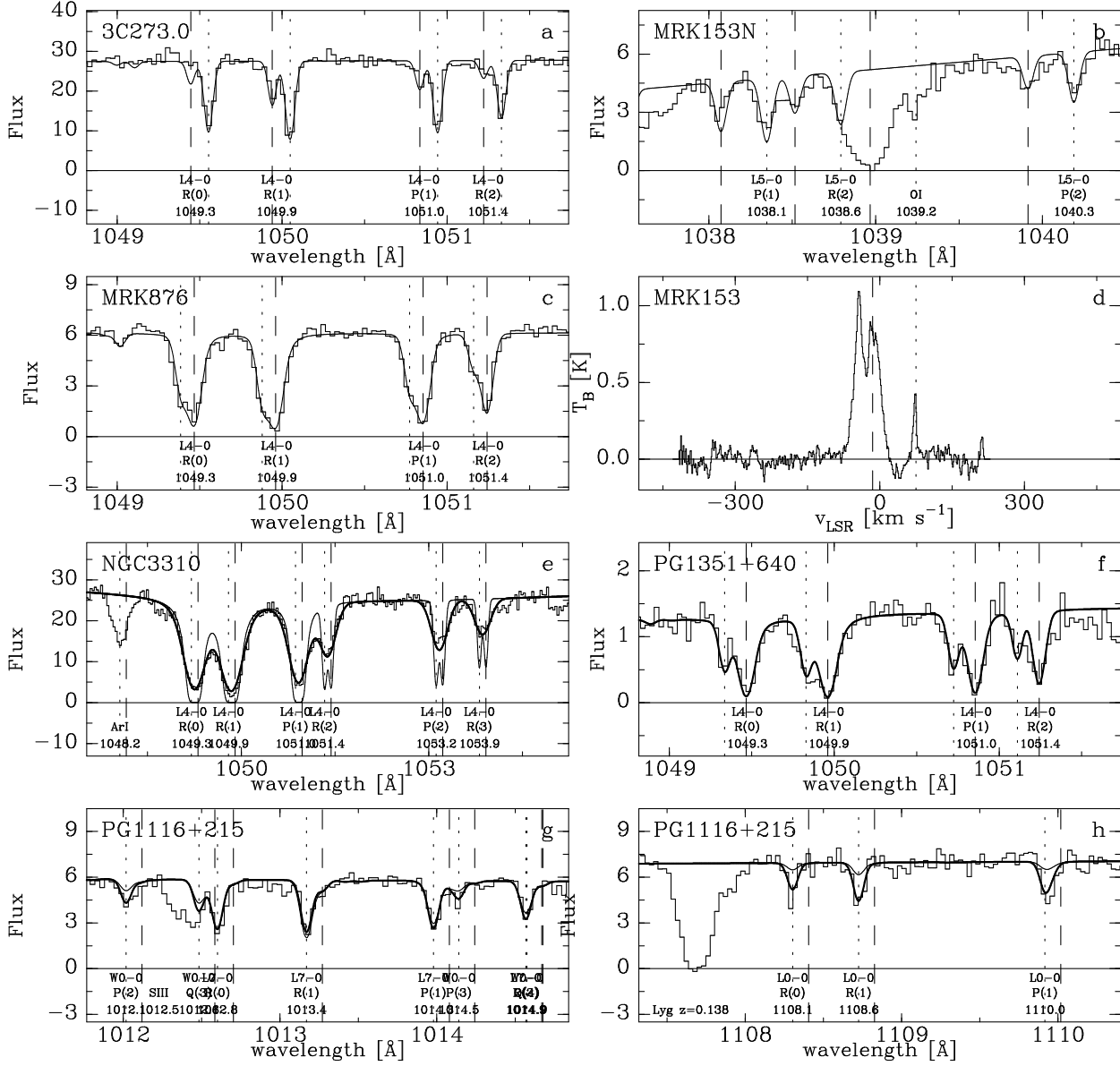


Fig. 2.— A series of examples for sightlines that are special cases. In all panels the low-velocity H₂ lines are indicated by dashed vertical lines, and intermediate-velocity H₂ absorption is shown by dotted vertical lines. (a) This panel shows that toward 3C273.0 a -9 km s^{-1} H₂ component is present, although Sembach et al. (2001a) claimed it was absent. (b, d) A narrow H I component is seen at 73 km s^{-1} toward Mrk 153. This component also shows up in O I $\lambda 1039.230$ and in H₂. (c) A special, well-studied IVC, the Draco Nebula ($v = -30 \text{ km s}^{-1}$), is detected toward Mrk 876 – it is seen as a weaker secondary component on the left of each H₂ line. (e). The two-component theoretical profiles toward NGC 3310 need to be smoothed by 80 km s^{-1} in order to represent the data, as shown by the thick lines; smoothing with the usual 20 km s^{-1} (thin lines) is clearly wrong. (g) This panel illustrates the highest column density ($\log N(\text{H}_2) = 16.45$) intermediate-velocity H₂ toward PG 1351+640). (g, h) These two panels compare the column densities and b -values for PG 1116+215 listed in Table 3 with those given by Richter et al. (2003); thick lines show the profiles implied by the parameters listed in Table 3, while the thin lines show the solution given by Richter et al. (2003). See

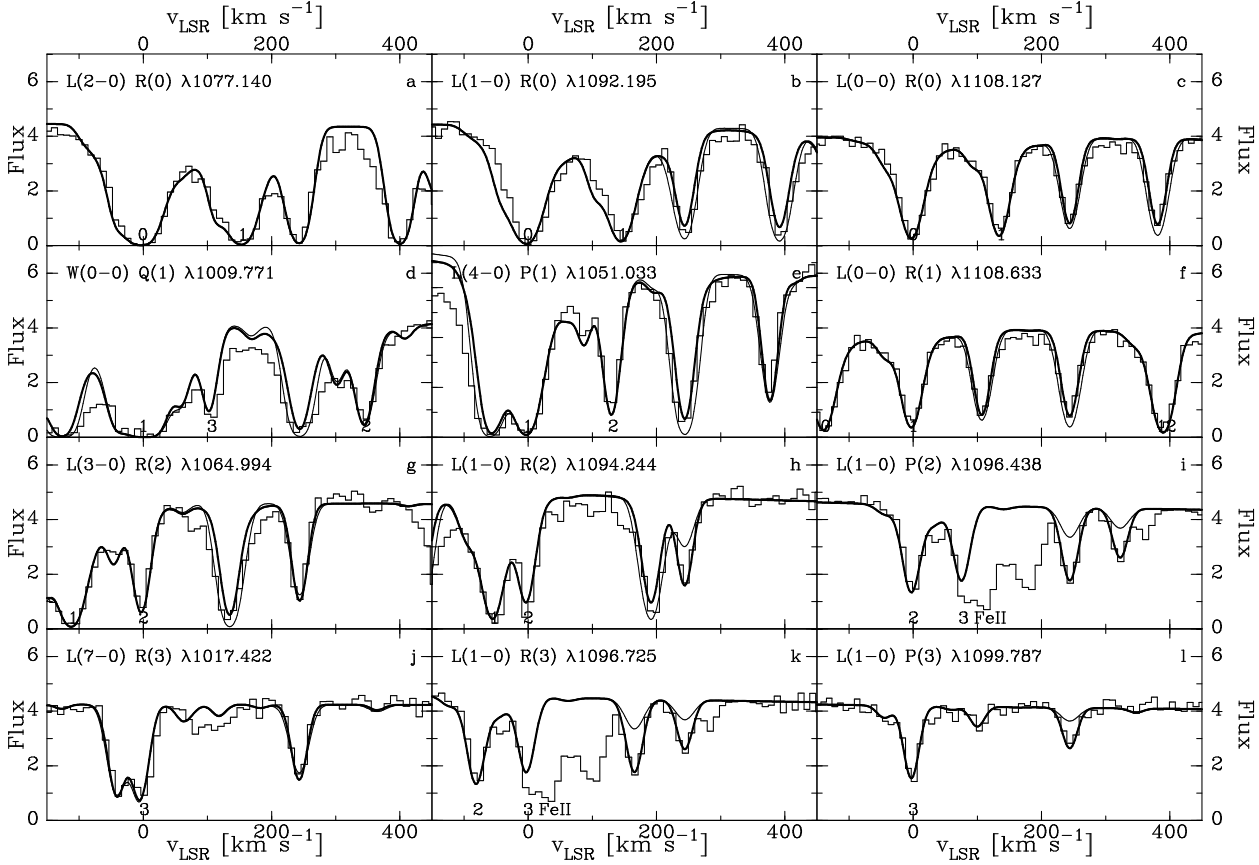


Fig. 3.— Examples of data and model fits for twelve H₂ lines in the spectrum of NGC 3783. The histograms show the data. Thick lines are the theoretical profiles implied by the high column density fit to the HVC at +244 km s⁻¹ that is preferred in this paper ($\log N(\text{H}_2)=18.17$, $\text{FWHM}=8.2$ km s⁻¹). Thin lines show the theoretical profiles implied by the fitted parameters in Sembach et al. (2001) ($\log N(\text{H}_2)=16.80$, $\text{FWHM}=20$ km s⁻¹). Clearly, the two predictions are very similar for most lines, but the Sembach et al. (2001) value underpredicts the absorption in the weakest $J=2$ and $J=3$ lines (panels h, i, k, l).

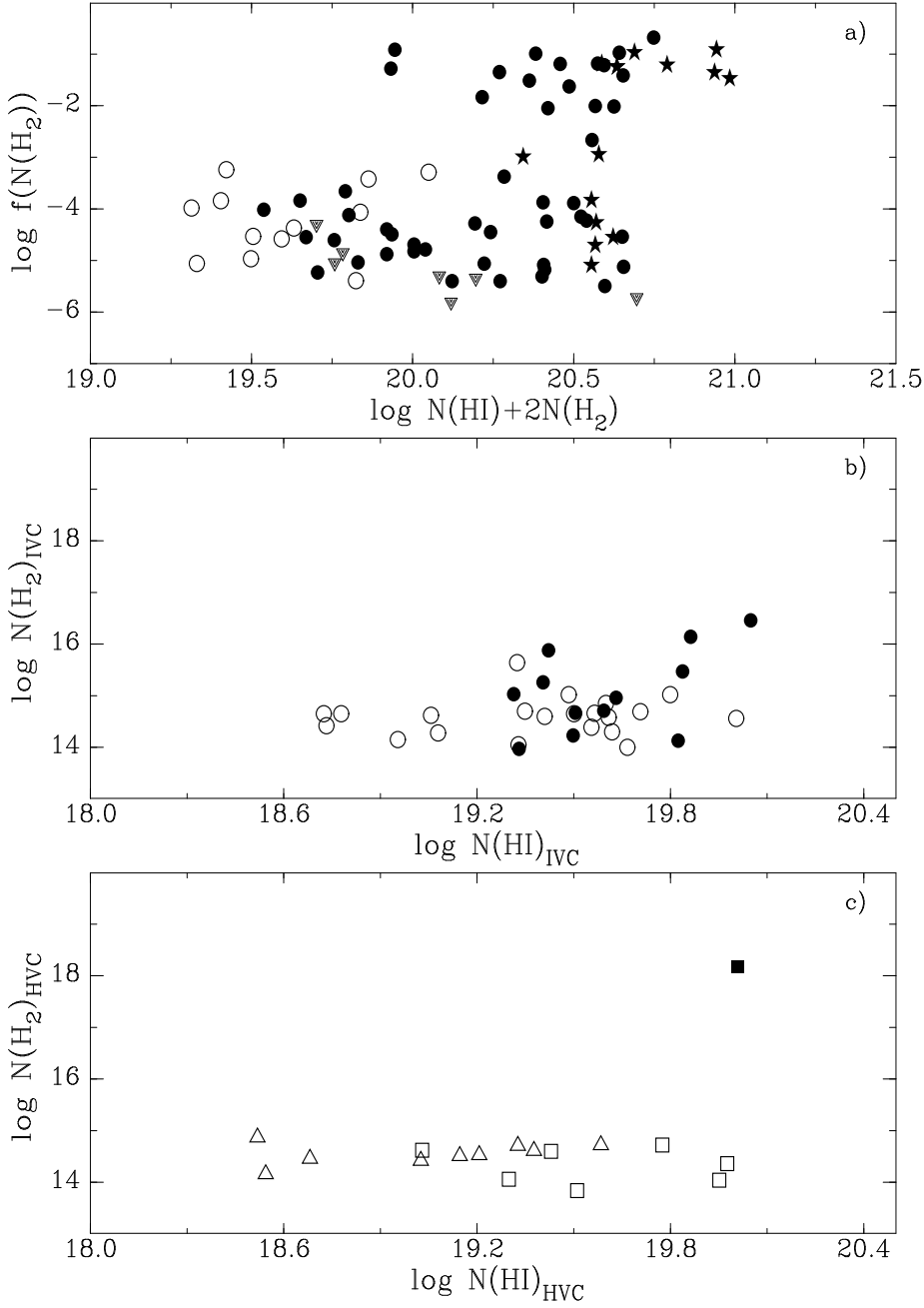


Fig. 4.— Panel (a) shows the correlation between total hydrogen column density and the fraction of H₂. Stars are for low-velocity gas at low latitudes ($|b| < 30^\circ$), closed circles for low-velocity gas at higher latitudes, triangles are for the sightlines with upper limits to $N(\text{H}_2)$, and open circles are for intermediate-velocity clouds. Panels (b) and (c) give the correlation between $\log N(\text{H I})$ and $\log N(\text{H}_2)$ in intermediate-velocity clouds (b) and high-velocity clouds (c). Closed circles/squares show detections. Open circles/squares/triangles show upper limits, with squares for complex C and triangles for other HVCs.

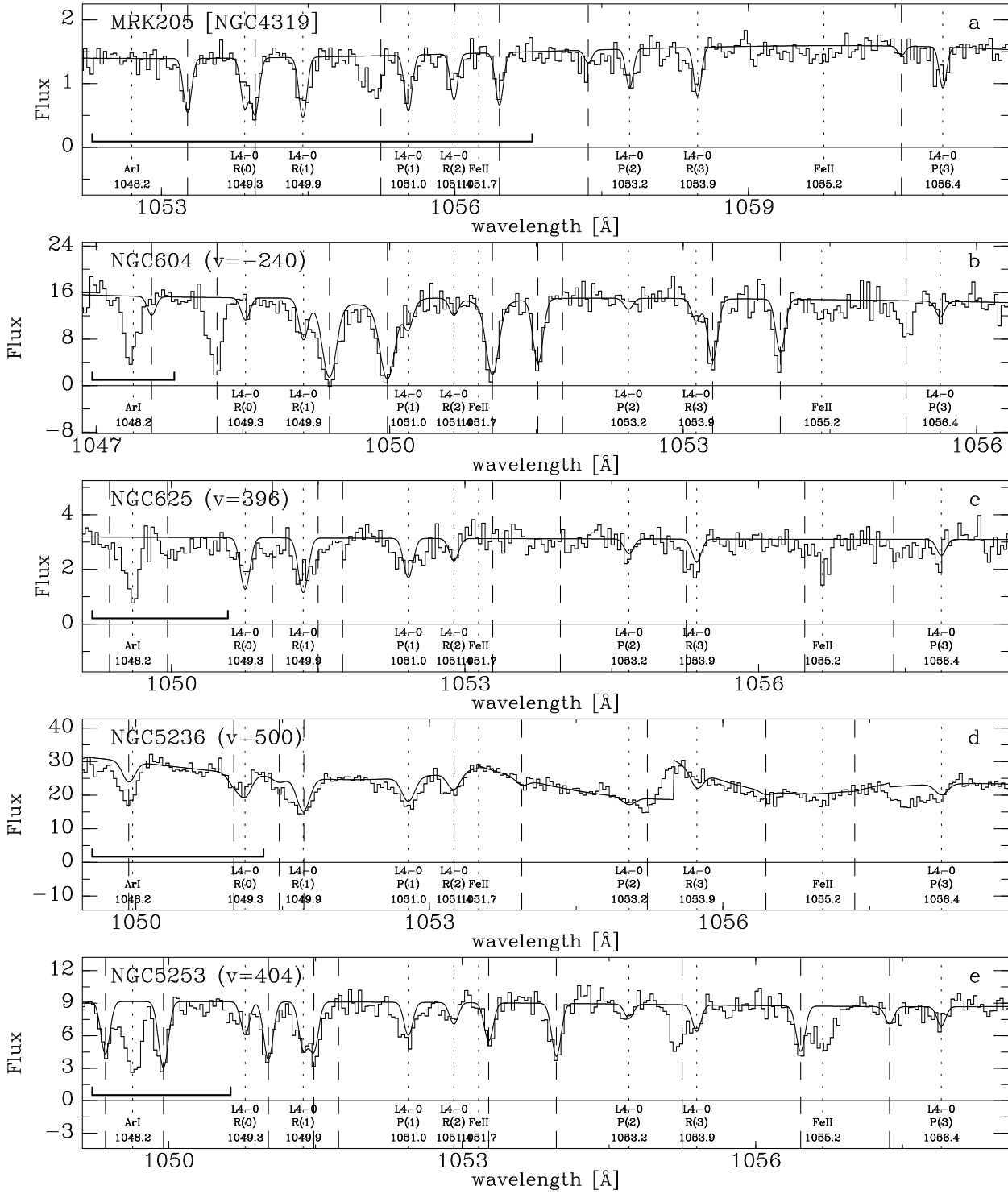


Fig. 5.— This figure shows lines in the L(4-0) band detected in five external galaxies. The spectra are aligned on the extragalactic H₂ line, which are labeled in each panel, and indicated by the dotted vertical lines. The dashed vertical lines show the positions of the Milky Way absorption lines. On the lower left sides, each panel also contains a horizontal bar, which shows the distance between each pair of Galactic and extragalactic absorption lines.

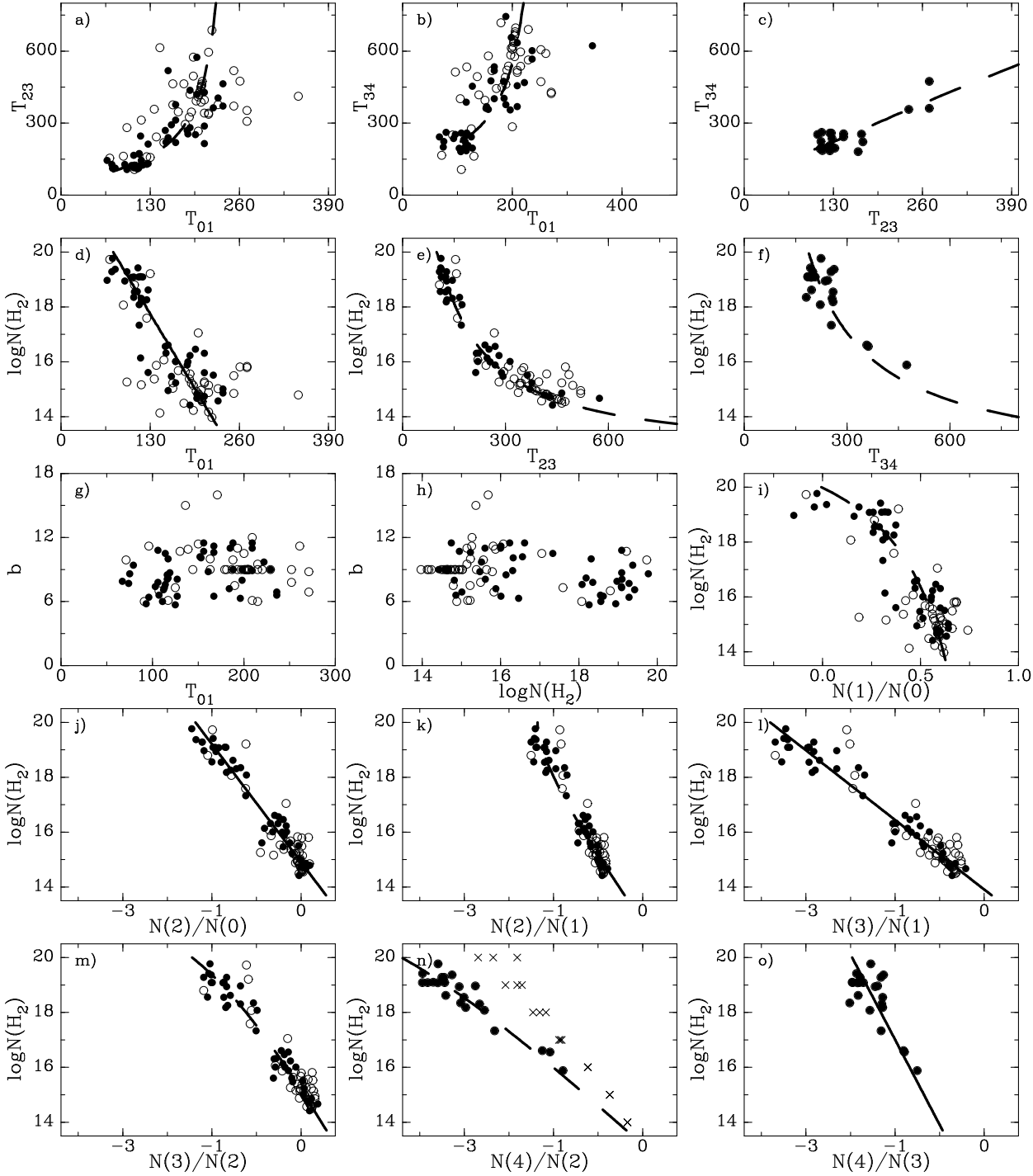


Fig. 6.— Scatter plots of the measured H_2 parameters. Filled circles are for the most reliable measurements (all in sightlines with S/N ratio >13), while open circles are for the remaining ones. The solid lines in panels d, j, l and o show the least-squares fits made to the filled circles in these plot. The dashed lines show the relations implied for the other scatter plots. Crosses in panel n show theoretical predictions from Browning et al. (2002). Note that panels d and i (T_{01} or $\log N(1)/N(0)$ vs $\log N(\text{H}_2)$) really display the same correlation, as do panel pairs e/m and f/o. Both are shown for convenience.

Table 1. Target Exposure List

object	lon [$^{\circ}$]	lat [$^{\circ}$]	type	dataset	Cal	T_{exp}	shifts					
					FUSE	[ks]	LiF1A	LiF1B	LiF2A	LiF2B	SiC2A	SiC2B
(1)	(2)	(3)	(4)	(5)	(6)	(7)	(8)	(9)	(10)	(11)	(12)	(13)
1H0707–495			Sey1	B1050101	2.4	20.3	–13	–13	–26	–26	–13	–13
				B1050102	2.4	24.2	–19	–19	–19	–19	–13	–13
				B1050103	2.4	22.5	–19	–19	–19	–19	–13	–13
1H0717+714	143.98	28.02	BLLac	Z9071301	2.4	47.6	14	14	3	14	3	–8
3C249.1	130.39	38.55	QSO	P1071601	2.1	11.4	16	16	7	7	50	50
				P1071602	2.1	9.5	25	–	–	–	50	50
				S6010901	2.1	30.7(25.7 ¹)	9	–	–5	–5	–5	–5
				P1071603	2.4	80.9	14	14	14	14	4	4
				D1170101 ³	2.4	20.8	17	17	–	–	–	–
				D1170102 ³	2.4	44.8	17	17	10	–	–	–
				D1170103 ³	2.4	21.3	17	17	–	–	–	–
3C273.0	289.95	64.36	QSO	P1013501	2.1	42.3	7	7	–5	–5	53	43
ESO141–G55	338.18	–26.71	Sey1	I9040104	2.4	40.4	–12	–12	–5	–5	–16	–24
ESO572–G34	286.12	42.12	IBm	B0220201	2.1	25.5	–6	–6	–10	–10	–25	–25
H1821+643	94.00	27.42	QSO	P1016402	2.4	62.7	29	29	29	29	17	17
				P1016405	2.4	27.2(21.7 ¹ ,23.0 ²)	21 ⁴	21	21	21 ⁴	–	–
				C0950201	2.4	104.5	26	26	–	–	13	13
				C0950202	2.4	85.8(93.1 ²)	34	34	–	–	–	–
HE0226–4110	253.94	–65.77	QSO	P2071301	2.1	11.0	–7	–10	–17	–13	7	7
				P1019101	2.1	64.3(50.3 ¹ ,49.9 ²)	–7	–10	–17	–13	–11	–11
				P1019102	2.4	14.5	–7	–10	–17	–13	–4	–4
				P1019103	2.4	18.9	–7	–10	–10	–13	–6	–6
				P1019104	2.4	18.1	–7	–10	–10	–13	–11	–11
				D0270101	2.4	23.9	–7	–4	–10	–3	–48	–48
				D0270102	2.4	39.9	–7	–4	–10	–3	–46	–46
				D0270103	2.4	17.2	–7	–15	–10	–3	–31	–61
HS0624+6907	145.71	23.35	QSO	P1071001	2.1	13.9	14	14	32	32	–	–
				P1071002	2.1	17.7	14	14	32	32	72	72
				S6011201	2.1	43.8	7	7	–5	–5	10	10
				S6011202	2.1	40.6	7	7	7	7	0	0
IC4662	328.55	–17.85	Irr	Z9090201	2.4	32.4	15	3	3	15	15	15
MRC2251–178	46.20	–61.33	QSO	P1111010	2.1	52.5	15	15	15	15	–17	–17
Mrk9	158.36	28.75	Sey1.5	P1071101	2.4	11.8	9	11	34	32	–	–
				P1071102	2.4	14.3	9	11	25	23	–	23
				P1071103	2.4	11.5(2.6 ¹)	9	–	0	3	14	14

Table 1—Continued

object	lon	lat	type	dataset	Cal	T_{exp}	shifts					
					FUSE		[ks]	LiF1A	LiF1B	LiF2A	LiF2B	SiC2A
(1)	(2)	(3)	(4)	(5)	(6)	(7)	(8)	(9)	(10)	(11)	(12)	(13)
				S6011601	2.1	23.9	9	–	0	3	–	–
Mrk59	111.54	82.12	HII(NGC4861)	A0360202	2.4	9.8	32	32	50	50	40	40
Mrk106	161.14	42.88	Sey1	C1490501	2.4	121.9(87.8 ²)	4	9	–	–	–	–
Mrk116	160.53	44.84	BCG	P1980102	2.4	31.6	8	8	43	43	–	–
				P1080901	2.4	63.5	15	–	15	15	3	3
Mrk153	156.73	56.01	Scp	A0940101	2.4	65.1	13	13	13	13	13	13
Mrk205	125.45	41.67	Sey1	Q1060203	2.4	35.5	14	14	14	14	20	20
				S6010801	2.1	16.8	14	14	0	0	–	–
				D0540101	2.4	20.7	10	10	10	10	–3	–3
				D0540102	2.4	112.4	10	10	10	10	–3	–3
				D0540103	2.4	20.9	10	10	10	10	–3	–3
Mrk209	134.15	68.08	BCD	P1072201	2.4	6.3	29	21	29	21	21	21
				Q2240101	2.4	19.3	21	21	21	21	9	9
Mrk279	115.04	46.86	Sey1.5	P1080303	2.4	61.2	24	24	24	24	34	34
				P1080304	2.4	30.7	24	24	35	35	26	26
				D1540101	2.4	91.4	21	21	21	21	15	5
Mrk290	91.49	47.95	Sey1	P1072901	2.1	12.8	17	17	17	17	–	–
				D0760101	2.4	9.3	17	20	14	25	–3	–3
				D0760102	2.4	47.1	17	20	14	11	–10	–10
				E0840101	2.4	11.5	17	20	6	3	6	6
Mrk335	108.76	–41.42	Sey1.2	P1010203	2.4	43.6(30.3 ¹)	16	16	47	47	–	–
				P1010204	2.1	53.4	16 ⁴	16	7	7 ⁴	–3	–3
Mrk421	179.83	65.03	BLLac	P1012901	2.1	21.8	11	11	3	3	3	3
				Z0100101	2.4	26.5	–3	–3	–22	3	–36	–36
				Z0100102	2.4	23.4	–3	–3	–22	3	–36	–36
				Z0100103	2.4	12.1	–3	–3	–22	3	–36	–36
Mrk477	93.04	56.82	Gal	D1180101	2.4	146.3	33	33	33	33	33	33
Mrk501	63.60	38.86	BLLac	P1073301	2.1	11.6	26	26	26	26	–	–
				C0810101	2.4	18.4	32	32	32	32	–20	–20
Mrk509	35.97	–29.86	Sey1.2	X0170101	2.4	19.4(14.9 ²)	8 ⁴	0 ⁴	23 ⁴	23 ⁴	30	30
				X0170102	2.4	32.5	25	18	–	–	–	–
				P1080601	2.1	61.1	12	12	18	18	–	–
Mrk586	157.60	–54.93	Sey1	D0550101	2.4	19.0	–10	–5	–10	–5	–16	–16
				D0550102	2.4	45.0	–5	–5	–10	–5	–25	–25
Mrk817	100.30	53.48	Sey1.5	P1080403	2.1	76.3	30	30	–	–	–	–

Table 1—Continued

object	lon [$^{\circ}$]	lat [$^{\circ}$]	type	dataset	Cal FUSE	T_{exp} [ks]	shifts					
							LiF1A	LiF1B	LiF2A	LiF2B	SiC2A	SiC2B
(1)	(2)	(3)	(4)	(5)	(6)	(7)	(8)	(9)	(10)	(11)	(12)	(13)
Mrk876	98.27	40.38	Sey1	P1080404	2.1	86.0	30	30	24	24	3	3
				P1073101	2.1	52.8	15 ⁴	15	12	12 ⁴	–	–
				D0280203	2.4	79.4	20	20	20	20	20	20
Mrk1095	201.69	–21.13	Sey1	P1011201	2.1	8.5	–13	–	–21	–21	–45	–45
				P1011202	2.1	21.0	–13	–	–21	–21	–10	–10
				P1011203	2.1	26.8	–21	–	–32	–42	12	–12
Mrk1383	349.22	55.12	Sey1	P1014801	2.1	25.5	28	28	13	13	89	89
				P2670101	2.1	39.0	28	28	28	28	28	28
Mrk1513	63.67	–29.07	Sey1	P1018301	2.4	22.7	15	15	11	11	36	36
				P1018302	2.4	11.9(10.5 ¹ ,10.2 ²)	30	30	30	30	15	15
				P1018303	2.4	8.3	26	26	26	26	26	26
				P1018304	2.4	22.0	9	9	9	9	13	13
MS0700.7+6338	152.47	25.63	Sey1	S6011501	2.4	16.9	9	–	0	0	5	5
				D0550501	2.4	82.1	9	9	9	9	14	14
				P2072701	2.4	7.4	9 ⁴	–	5	5	–	–
NGC604	133.76	–31.18	HII(M33)	B0180201 ³	2.4	12.9	16 ⁴	16	3	10	9	9
NGC625	273.67	–73.12	SBm	D0400101 ³	2.4	56.7	–4	0	–10	0	–26	–26
NGC985	180.84	–59.49	Sey1	P1010903	2.4	68.0(50.6 ¹ ,44.3 ²)	3	3	–	–	59	59
NGC1068	172.10	–51.93	Sey1	P1110202	2.1	22.6	–10	–10	–24	–24	–3	–3
NGC1399	236.72	–53.63	cD/E1	A0880303	2.4	16.5	–12	–12	–12	–12	–12	–12
				A0880304	2.4	11.8(9.0 ¹ ,8.8 ²)	–26	–26	–26	–26	–12	–12
NGC1522	262.00	–45.97	S0pec	Z9090501	2.4	40.3	–11	–11	–19	–19	–31	–31
NGC1672	268.78	–38.99	Sey2	C1090101	2.4	4.3	–3	–3	–18	–18	0	0
				C1090103	2.4	8.0	–3	–3	–18	–18	0	0
				C1090104	2.4	20.2	–3	–3	–	–	0	0
				C1090105	2.4	21.6	–3	–3	–18	–18	0	0
NGC1705	261.08	–38.74	SA0pec	A0460102	2.4	8.6	–21	–21	–32	–32	–21	–21
				A0460103	2.4	15.4	–21	–21	–32	–32	–21	–21
NGC3310	156.60	54.06	SABbc	A0460201	2.1	27.1	0	0	0	0	0	0
NGC3690	141.91	55.41	IBm	B0040201	2.1	16.1	10	20	10	20	20	20
				B0040202	2.1	43.6	28	28	38	38	–53	–53
NGC3783	287.46	22.95	Sey1	P1013301	2.4	37.3(19.5 ²)	5	5	–6	–6	45	45
				B1070102	2.4	27.8	6	6	6	6	6	6
				B1070106	2.4	26.4	6	6	6	6	9	9
				B1070103	2.4	27.5	4	–	7	7	7	7

Table 1—Continued

object	lon [$^{\circ}$]	lat [$^{\circ}$]	type	dataset	Cal FUSE	T_{exp} [ks]	shifts					
							LiF1A	LiF1B	LiF2A	LiF2B	SiC2A	SiC2B
(1)	(2)	(3)	(4)	(5)	(6)	(7)	(8)	(9)	(10)	(11)	(12)	(13)
				B1070104	2.4	24.1	3	–	3	3	3	3
				B1070105	2.4	27.5(17.3 ¹)	–1	–1	–10	–10	–14	–14
				E0310101	2.4	25.0	3	3	–4	–4	–36	–36
NGC4051	148.88	70.09	Sey1.5	B0620201	2.1	28.7	15	15	15	15	15	15
				C0190101	2.4	34.7	15	15	15	15	15	15
				C0190102	2.4	28.8	15	–	15	15	15	15
NGC4151	155.08	75.06	Sey1.5	C0920101	2.1	54.3(34.5 ¹)	19	25	19	19	–36	–36
NGC4214	160.24	78.07	IABm	A0460303	2.4	20.7(11.4 ¹)	12	12	12	12	62	62
NGC4449	136.88	72.41	IBm	A0460606	2.4	8.5	–5	–5	–5	–5	–20	–20
NGC4449–HII	136.88	72.41	HII(4449)	A0460707	2.4	14.1	3	3	3	3	–33	–33
NGC4670	212.69	88.63	BCD	B0220301	2.1	8.7	8	8	8	8	8	8
				B0220302	2.1	16.0	8	8	8	8	20	20
				B0220303	2.1	10.7	8	8	8	8	8	8
NGC5236	314.58	31.97	SABc	A0460505	2.4	26.5	–13	–13	–2	–2	–18	–18
NGC5253	314.86	30.10	Im	A0460404 ³	2.4	27.4	–7	–7	–7	–7	–7	–7
NGC5408	317.15	19.50	IBm	Z9090901	2.4	16.9(18.5 ²)	30	30	15	15	30	–10
NGC7469	83.10	–45.47	Sey1.2	P1018703	2.4	36.0	22	22	52	52	–	–
NGC7714	88.22	–55.56	SBB;HII	A0230404	2.1	8.8(5.7 ^{1,2})	13	0	–5	–5	0	0
				A0860606	2.1	6.0	20	20	–2	–2	3	3
				B0040301	2.1	16.7	11	7	3	3	–13	–13
				C0370201 ³	2.0	51.2	7	7	3	3	–	21
				C0370202 ³	2.0	10.1	–	7	3	3	–	–
				C0370204 ³	2.0	18.8	–	7	3	3	–	–
				C0370206 ³	2.4	11.9(10.3 ^{1,2})	9	9	–10	–10	–	–
PG0804+761	138.28	31.03	QSO	P1011901	2.1	57.5(38.2 ¹)	13 ⁴	7	7	10 ⁴	–	–
				P1011903	2.4	21.1	18	18	35	35	68	58
				S6011001	2.1	58.5	8	8	0	0	–16	–16
				S6011002	2.1	36.9	8	8	0	0	3	3
PG0844+349	188.56	37.97	Sey1	P1012002	2.1	31.1	–2	–2	–12	–12	56	45
				D0280301	2.4	11.3(8.7 ²)	3	–2	3	6	–	–
				D0280302	2.4	12.3(0.0 ²)	3	6	–	–	–	–
				D0280303	2.4	12.3(3.3 ²)	3	6	–	–	–	–
				D0280304	2.4	14.7	3	6	3	6	–	–
PG0953+414	179.79	51.71	QSO	P1012201	2.1	34.1	10	5	5	5	14	14
				P1012202	2.4	38.0	5	5	5	5	14	14

Table 1—Continued

object	lon [$^{\circ}$]	lat [$^{\circ}$]	type	dataset	Cal FUSE	T_{exp} [ks]	shifts					
							LiF1A	LiF1B	LiF2A	LiF2B	SiC2A	SiC2B
(1)	(2)	(3)	(4)	(5)	(6)	(7)	(8)	(9)	(10)	(11)	(12)	(13)
PG1011–040	246.50	40.75	Sey1	B0790101	2.4	86.3	0	0	–10	–10	–13	–20
PG1116+215	223.36	68.21	QSO	P1013101	2.1	11.0	3	3	–5	–5	–14	–14
				P1013102	2.1	11.1	3	3	–5	–5	–14	–14
				P1013103	2.1	8.5	3	3	–5	–5	–18	–18
				P1013104	2.1	11.2	3	3	–5	–5	–14	–14
				P1013105	2.1	35.1	3	3	–5	–5	–18	–18
PG1211+143	267.55	74.32	Sey1	P1072001	2.4	52.3	6	6	–9	–9	32	25
PG1259+593	120.56	58.05	QSO	P1080102	1.8	57.9	14	–6	–22	0	0	in
PG1302–102	308.59	52.16	QSO	P1080201	2.1	32.0	5	5	5	–	31	–
				P1080202	2.1	31.8	5	5	–	–	–	–
				P1080203	2.1	81.1	16	21	8	8	8	–
PG1351+640	111.89	52.02	Sey1	P1072501	2.1	70.2	30	30	30	30	30	30
				S6010701	2.1	50.5	30	30	20	20	5	5
PG1553+113	21.91	43.96	BLLac	E5260501	2.4	13.6(12.0 ¹ ,10.8 ²)	26	31	34	34	9	9
				E5260502	2.4	22.1(18.1 ²)	26	31	34	34	9	9
				E5260503	2.4	15.0	26	31	34	34	9	9
PG1626+554	84.51	42.19	Sey1	C0370101 ³	2.1	91.2	30	30	30	30	0	–
PHL1811	47.47	–44.81	QSO	P2071101	2.4	11.3	19	19	8	14	4	4
				P1081001	2.4	10.4(16.0 ¹ ,15.9 ²)	19	19	–	–	–	–
				P1081002	2.4	11.8(25.6 ¹ ,24.2 ²)	19	19	–	–	–35	–
				P1081003	2.4	14.2(23.2 ¹ ,22.8 ²)	19	19	19	–	–35	–35
PKS0405–12	204.93	–41.76	QSO	B0870101	2.1	71.1	–6	–6	–17	–17	–7	–7
				D1030101	2.4	34.5	–1	–1	–5	–1	19	19
				D1030102	2.4	34.9	–1	–1	–5	–1	19	19
PKS0558–504	257.96	–28.57	QSO	P1011504	2.4	45.5	–15	–15	33	33	–15	–15
				C1490601	2.4	47.9	–21	–21	–21	–21	–15	–15
PKS2005–489	350.37	–32.60	BLLac	P1073801	2.1	12.3	4	–	4	4	–15	–15
				C1490301	2.1	23.5	9	9	9	9	–15	–
				C1490302	2.1	13.4	9	–	9	9	–	–
PKS2155–304	17.73	–52.25	BLLac	P1080701	2.1	19.2	4	4	–7	–7	–	–
				P1080705	2.1	38.6	4	4	–7	–7	–	–
				P1080703	2.1	65.4	8	8	3	3	–11	–7
TonS180	139.00	–85.07	Sey1.2	P1010502	2.4	16.6	–2	–2	50	50	65	35
				D0280101	2.4	12.0	14	14	–2	–2	–2	35
TonS210	224.97	–83.16	QSO	P1070301	2.1	13.5	–20	–20	–	–	–	–

Table 1—Continued

object	lon [$^{\circ}$]	lat [$^{\circ}$]	type	dataset	Cal	T_{exp}	shifts					
					FUSE	[ks]	LiF1A	LiF1B	LiF2A	LiF2B	SiC2A	SiC2B
(1)	(2)	(3)	(4)	(5)	(6)	(7)	(8)	(9)	(10)	(11)	(12)	(13)
VII Zw118	151.36	25.99	Sey1	P1070302	2.1	41.0(32.6 ¹ ,31.8 ²)	–4	–4	–11	–11	–50	–50
				P1011604	2.1	79.6(46.5 ¹)	6 ⁴	–	6	6 ⁴	–	–
				P1011605	2.4	26.1	11	11	40	40	–	–
				P1011606	2.4	9.8	11	11	11	11	13	–
				S6011301	2.1	49.9	11	11	–	0	–7	–7

Note. — See Sects. 2.1 and 2.2 for a detailed description of the columns; 1: Useable exposure time in LiF1A segment >10% less than nominal time; 2: Useable exposure time in LiF2A segment >10% less than nominal time; 3: Observed in the MDRS aperture, rather than in the LWRS aperture; 4: Observations for which some segments show a clear slope in the centroid vs wavelength plot; specifically (in units of $\text{km s}^{-1}/\text{\AA}$): ESO141-G55-I9040104 (1999 10 16): 1alif=–0.1206, 1blif=–0.2395, 2alif=–0.2336, 2blif=–0.1094; H1821+643–P1016405 (1999 10 13): 1alif=–0.1108, 2blif=–0.1643; Mrk335–P1010204 (2000 11 21): 1alif=0.1179, 2blif=–0.1113; Mrk509–X0170101 (1999 11 02): 1alif=–0.1539, 1blif=–0.1590, 2alif=–0.2923, 2blif=–0.1565; Mrk876–P1073101 (1999 10 16): 1alif=–0.1383, 2blif=–0.1597; MS0700.7+6338–P2072701 (2000 01 10): 1alif=0.1721; NGC604–B0180201 (2001 09 03): 1alif=–0.1876; PG0804+761–P1011901 (1999 10 05): 1alif=–0.1691, 2blif=–0.1149; VII Zw118–P1011604 (1999 10 06): 1alif=–0.1149, 2blif=–0.1377.

Table 2. S/N ratios

object	Flux	S/N	S/N	S/N	S/N	$v(\text{HI})$	$v(\text{metal})$	$v(\text{H}_2)$	instr
	[f.u.] ¹	1031	1063	977	1122	[km s ⁻¹]	[km s ⁻¹]	[km s ⁻¹]	
(1)	(2)	(3)	(4)	(5)	(6)	(7)	(8)	(9)	(10)
1H0707–495	1.76	11.66	12.02	4.04	8.27	–1,61	2,61	–1	21cm–H2
1H0717+714	2.70	11.69	12.69	4.57	12.25	–51,–5	–51,–5	–51,–5	21cm
3C249.1	1.10	13.75	12.12	3.36	12.68	–50,9	–47,–2	3	E140M
3C273.0	26.86	31.16	25.38	19.24	39.03	–6,25	–14,22	–9,28	E140M
ESO141–G55	5.17	15.96	22.96	7.78	19.96	–45,–1	–1	–4	21cm
ESO572–G34	6.39 ^a	11.21	13.83	4.51	14.58	–4,0	–4	–4	21cm
H1821+643	3.04	27.89	23.97	7.47	26.09	–128,–87,–3	–129,–82,–13	–5	E140M
HE0226–4110	2.73	24.59	21.23	10.97	18.41	–7,0	–4	–7	E140M
HS0624+6907	0.96	11.03	11.19	2.65	12.64	–100,0	–5	–5	E140M
IC4662	4.96 ^a	13.33	12.95	9.09	14.52	3,100,317	–21,317		21cm
MRC2251–178	2.15	11.56	11.08	2.66	11.63	0,59	0	0	21cm
Mrk9	2.26	12.63	10.53	2.39	13.66	–40,–3	–3	–3	21cm
Mrk59	22.19 ^a	13.95	15.42	7.97	18.33	–44,–20,–1	<–11> ²	–44,–1	21cm
Mrk106	1.62	12.09	10.49	3.30	9.79	–157,–39,–6	–157,–42,–6	–6	21cm
Mrk116	2.82 ^a	15.23	15.67	5.54	16.48	–170,–39,7	–39,7	9	21cm
Mrk153	7.76 ^a	15.18	20.80	9.91	26.84	–43,–20,–9,73	–43,–20,74	–20,75	21cm
Mrk205	1.27	15.88	16.40	5.71	19.75	–202,–120,–48,2	–207,–59,–16	–5,1281	E140M
Mrk209	4.99 ^a	10.05	12.44	4.71	15.11	–99,–56,–9,288	–9,–49,295		21cm
Mrk279	10.15	44.13	42.95	20.62	41.09	–137,–76,–40,4	–146,–76,–2		E140M
Mrk290	3.39	18.52	25.70	5.78	14.20	–138,–105,–5	–138,–13	–13	21cm
Mrk335	7.06	27.05	32.26	11.32	22.64	–27,–3	–42,–3	–6	21cm
Mrk421	9.62	29.15	27.33	14.39	21.24	–60,–8	–60,–19	–60,–19	21cm
Mrk477	0.99	10.21	4.90	2.08	8.86	–38,–5	–5	–5	21cm
Mrk501	3.10	9.94	9.45	3.05	10.71	–116,–83,2	–116,–83,–4	2	21cm
Mrk509	6.66	29.47	27.83	6.99	22.71	–7,6,60	0,60	–1,60	E140M
Mrk586	2.09	11.94	11.55	3.86	11.54	–11,0	–11	–11	21cm
Mrk817	9.59	41.52	45.40	18.24	30.55	–109,–40,–5	–109,–38,–5	–40,–5	21cm
Mrk876	6.32	33.26	35.69	10.69	23.47	–173,–133,–30,–7	–121,–30,–11	–30,–2	E140M
Mrk1095	2.00	10.99	20.55	4.40	10.45	0,9	0	9	21cm–H2
Mrk1383	6.61	23.11	24.98	11.76	30.90	–2,0	–2	–2	21cm
Mrk1513	3.88	16.30	14.04	6.07	17.61	0,1	1	–25,6	21cm
MS0700.7+6338	1.87	14.61	12.56	4.18	14.56	–1,0	–9	–1	21cm–H2
NGC604	14.13 ^a	11.16	14.07	3.83	14.45	–259,0	0	–240,5	21cm
NGC625	2.70 ^a	10.99	12.05	1.97	10.56	0,0	0	396	21cm
NGC985	3.35	10.67	12.15	5.13	10.43	–8,0	–8	–2	21cm

Table 2—Continued

object	Flux [f.u.] ¹	S/N 1031	S/N 1063	S/N 977	S/N 1122	$v(\text{HI})$ [kms ⁻¹]	$v(\text{metal})$ [kms ⁻¹]	$v(\text{H}_2)$ [kms ⁻¹]	instr
(1)	(2)	(3)	(4)	(5)	(6)	(7)	(8)	(9)	(10)
NGC1068	12.32 ^a	29.30	19.62	11.40	21.43	-58,-6,5	-54,-4	5	21cm-H2
NGC1399	4.67 ^a	4.53	11.28	2.91	12.77	-9,0	-9		21cm
NGC1522	4.77 ^a	8.98	11.93	4.57	13.76	0,0		0	
NGC1672	2.62 ^a	5.15	10.44	3.72	10.88	0,92,168	0		21cm
NGC1705	36.80 ^a	26.74	32.83	14.72	30.20	19,88,285	-5		E140M
NGC3310	26.08 ^a	21.67	25.49	8.41	34.49	-47,-17	-48,-17	-47,-17	21cm
NGC3690	5.57 ^a	17.93	23.80	4.41	24.36	-100,-54,0	[-27] ³		21cm-H2
NGC3783	5.01 ^a	23.54	27.38	12.89	23.45	-2,62,242	-7,62,242	-45,-3,244	E140M
NGC4051	1.31 ^a	16.59	9.92	4.08	9.29	-57,-14	-49,-16	-49,-14	E140M
NGC4151	29.03 ^a	32.93	31.66	18.42	31.21	-41,-21,0	-21	-21	E140M
NGC4214	28.16 ^a	16.01	19.04	9.02	28.68	-33,-2,295	-33,-5	-5	21cm
NGC4449	21.29 ^a	9.69	15.00	4.40	16.72	-45,-12,214	<-28> ⁴		21cm
NGC4449-HII	46.77 ^a	24.77	25.28	8.57	28.38	-45,-11,221	<-27> ⁴	-28	21cm
NGC4670	10.78 ^a	16.73	22.09	5.47	24.12	-28,-8,0	<-17> ⁵	-8	21cm
NGC5236	24.05 ^a	20.25	27.71	8.30	27.32	-9,0	-9	-9,500	21cm
NGC5253	8.82 ^a	11.63	16.04	2.34	20.55	-6,102	-17,102	-4,404	21cm
NGC5408	5.40 ^a	7.47	10.09	2.83	10.93	-7,0	-7	4	21cm
NGC7469	5.93	16.03	15.86	0.54	17.97	-333,-3	-337,-3	-3	21cm
NGC7714	2.53 ^a	12.78	14.97	4.50	16.32	-316,-50,-3	-2	-50,-5	21cm
PG0804+761	7.01	30.61	25.10	14.08	41.65	-58,6	-58,-13	-8	21cm
PG0844+349	3.74	20.00	18.86	6.60	20.21	0,6	2	6	21cm-H2
PG0953+414	5.15	24.29	20.98	10.24	26.80	-49,-4	-50,-8	-26,1	E140M
PG1011-040	2.62	17.24	15.23	6.97	16.64	-5,123	-5,123	-5	21cm
PG1116+215	5.67	25.54	23.63	11.80	20.12	-42,-7	-44,-11,56,184	-44,-11	E140M
PG1211+143	5.44	18.95	18.75	9.53	27.02	-35,-9	-36,-19,-8	-12	E140M
PG1259+593	1.79	37.29	24.00	13.80	23.87	-128,-54,-6	-128,-56,-2	-54,3	E140M
PG1302-102	1.63	15.67	15.98	4.82	15.94	-1,0	0	-9	E140M
PG1351+640	1.62	15.88	13.64	3.96	18.79	-156,-47,-1	-151,-47,-2	-47,-2	21cm
PG1553+113	2.72	11.88	14.50	3.68	13.64	0,1	1	6	21cm
PG1626+554	1.47	14.13	12.46	0.00	11.52	-121,-4	-121,-4	-4	21cm
PHL1811	4.91	17.11	17.22	-0.01	18.86	-5,0,5	0	0	E140M
PKS0405-12	2.18	18.63	16.30	6.77	18.76	0,1	-44,5	4	E140M
PKS0558-504	3.29	18.80	16.13	9.28	23.33	4,27,71	4	1	21cm
PKS2005-489	4.96	17.53	15.16	8.23	14.64	0,2	2,67	2	21cm
PKS2155-304	12.75	31.72	33.30	12.41	26.16	-4,0	-4	-7	E140M

Table 2—Continued

object	Flux [f.u.] ¹	S/N 1031	S/N 1063	S/N 977	S/N 1122	$v(\text{HI})$ [km s ⁻¹]	$v(\text{metal})$ [km s ⁻¹]	$v(\text{H}_2)$ [km s ⁻¹]	instr
(1)	(2)	(3)	(4)	(5)	(6)	(7)	(8)	(9)	(10)
TonS180	6.35	13.57	13.56	5.57	13.92	-6,0	-6		21cm
TonS210	6.23	20.16	19.29	8.40	16.61	-10,0	-10	-10	E140M
VIIZw118	2.01	18.27	18.00	5.44	26.22	-3,0	-1	-3	21cm

Note. — See Sect 2.2 for a detailed description of the columns; 1: flux in units of $10^{-14} \text{ erg cm}^{-2} \text{ s}^{-1} \text{ \AA}^{-1}$ – an (a) indicates the flux value is for 1063 \AA , instead of 1031 \AA ; 2: average between -20 and -1 km s^{-1} ; 3: uncertain velocity – broad ISM lines without easily recognizable components; 4: average between -11 and -45 km s^{-1} ; 5: average between -26 and -8 km s^{-1} ;

Table 3. H₂ measurements

object	$v(\text{H}_2)$ [km s ⁻¹]	$N(\text{J}=0)$	$N(\text{J}=1)$	$N(\text{J}=2)$	$N(\text{J}=3)$	$N(\text{J}=4)$	$N^a(\text{H}_2)$	W^b [km s ⁻¹]	W_f^c [km s ⁻¹]	T_{01}^d [K]	T_{23}^d [K]	T_{34}^d [K]
(1)	(2)	(3)	(4)	(5)	(6)	(7)	(8)	(9)	(10)	(11)	(12)	(13)
1H0707–495	–1	14.73 ^{+0.41} _{–0.26}	15.29 ^{+0.71} _{–0.38}	14.68 ^{+0.34} _{–0.26}	14.78 ^{+0.36} _{–0.25}	<14.56	15.56 ^{+0.51} _{–0.18}	9.9 ^{+5.0} _{–1.9}	lin	188	420	(462)
	61	<14.35	<14.48	<14.50	<14.50	<14.44	<14.59	(9.0)	–			
1H0717+714	–51	14.12 ^{+0.16} _{–0.18}	14.71 ^{+0.22} _{–0.23}	<14.56	<14.52	<14.52	14.96 ^{+0.18} _{–0.17}	9.0 ^{+0.0} _{–0.0}	lin	204	(387)	(577)
	–5	16.28 ^{+0.74} _{–0.27}	16.87 ^{+0.76} _{–0.40}	16.06 ^{+0.78} _{–0.30}	15.87 ^{+0.77} _{–0.28}	14.48 ^{+0.19} _{–0.14}	17.04 ^{+0.63} _{–0.22}	10.5 ^{+2.5} _{–2.5}	–	200	267	285
3C249.1	–50	<15.13	<15.72	<14.30	<14.27	<14.20	<15.01	(9.0)	–			
	3	18.58 ^{+0.07} _{–0.05}	18.91 ^{+0.05} _{–0.05}	17.48 ^{+0.16} _{–0.14}	16.34 ^{+0.12} _{–0.17}	14.57 ^{+0.20} _{–0.21}	19.09 ^{+0.03} _{–0.03}	8.7 ^{+0.5} _{–0.5}	–	119	125	207
3C273.0	–9	13.94 ^{+0.10} _{–0.11}	14.58 ^{+0.13} _{–0.11}	14.01 ^{+0.10} _{–0.10}	14.16 ^{+0.10} _{–0.09}	<13.79	14.86 ^{+0.07} _{–0.06}	6.6 ^{+1.1} _{–0.8}	6.0	236	464	(602)
	28	15.14 ^{+0.12} _{–0.12}	15.69 ^{+0.01} _{–0.11}	14.90 ^{+0.07} _{–0.07}	14.71 ^{+0.07} _{–0.06}	13.73 ^{+0.10} _{–0.13}	15.88 ^{+0.02} _{–0.07}	7.2 ^{+0.2} _{–0.2}	7.4	184	270	474
ESO141–G55	–4	18.88 ^{+0.10} _{–0.10}	19.06 ^{+0.12} _{–0.14}	17.47 ^{+0.29} _{–0.72}	16.05 ^{+0.60} _{–0.47}	14.53 ^{+0.20} _{–0.20}	19.28 ^{+0.08} _{–0.08}	6.4 ^{+1.1} _{–0.7}	–	96	107	253
ESO572–G34	–4	<14.24	14.64 ^{+0.51} _{–0.31}	14.08 ^{+0.25} _{–0.21}	<14.43	<14.32	14.93 ^{+0.44} _{–0.22}	(9.0)	7.2	(197)	(392)	(584)
H1821+643	–128	<13.79	<13.98	<14.02	<13.99	<14.02	<14.15	(9.0)	–			
	–87	<13.79	<13.97	<13.99	<13.99	<14.03	<14.14	(9.0)	–			
	–5	15.26 ^{+0.21} _{–0.12}	15.82 ^{+0.22} _{–0.09}	14.98 ^{+0.28} _{–0.16}	14.74 ^{+0.18} _{–0.13}	<14.04	15.99 ^{+0.16} _{–0.06}	11.0 ^{+2.0} _{–2.0}	7.2	185	255	(403)
HE0226–4110	–7	13.68 ^{+0.19} _{–0.22}	14.31 ^{+0.25} _{–0.20}	13.81 ^{+0.17} _{–0.18}	13.89 ^{+0.16} _{–0.16}	<14.07	14.56 ^{+0.15} _{–0.10}	(9.0)	lin	229	405	(690)
HS0624+6907	–100	<15.39	<15.87	<14.85	<14.62	<14.59	<15.63	(9.0)	–			
	–5	19.46 ^{+0.05} _{–0.03}	19.37 ^{+0.07} _{–0.04}	18.14 ^{+0.14} _{–0.12}	17.34 ^{+0.09} _{–0.39}	15.23 ^{+0.57} _{–0.30}	19.73 ^{+0.03} _{–0.02}	9.9 ^{+2.4} _{–2.1}	lin	71	154	166
IC4662	15	<14.91	<14.56	<14.50	<14.53	<14.54	<14.66	(9.0)	–			
	100	<14.34	<14.50	<14.47	<14.50	<14.35	<14.61	(9.0)	–			
	317	<14.35	<14.46	<14.42	<14.49	<14.38	<14.57	(9.0)	–			
MRC2251–178	0	14.15 ^{+0.33} _{–0.33}	14.78 ^{+0.51} _{–0.30}	<14.52	<14.56	<14.46	15.02 ^{+0.45} _{–0.23}	(9.0)	lin	229	(377)	(563)
	59	<14.32	<14.54	<14.52	<14.41	<14.39	<14.64	(9.0)	–			
Mrk9	–40	<15.07	<15.52	<14.14	<14.50	<14.42	<14.84	(9.0)	–			
	–3	18.94 ^{+0.08} _{–0.07}	19.23 ^{+0.07} _{–0.07}	17.65 ^{+1.16} _{–0.74}	16.30 ^{+0.67} _{–0.50}	14.43 ^{+0.25} _{–0.26}	19.41 ^{+0.10} _{–0.05}	7.1 ^{+0.3} _{–0.3}	8.6	112	111	193
Mrk59	–44	14.27 ^{+0.12} _{–0.14}	14.77 ^{+0.18} _{–0.18}	<14.33	<14.35	<14.28	15.02 ^{+0.14} _{–0.13}	9.0 ^{+0.0} _{–0.0}	lin	163	(376)	(562)
	–1	14.40 ^{+0.23} _{–0.23}	15.00 ^{+0.39} _{–0.38}	14.32 ^{+0.25} _{–0.26}	14.30 ^{+0.14} _{–0.18}	<14.39	15.22 ^{+0.27} _{–0.19}	6.1 ^{+0.9} _{–0.3}	lin	209	342	(520)
Mrk106	–156	<14.35	<14.62	<14.61	<14.53	<14.58	<14.72	(9.0)	–			
	–40	<15.46	<14.60	<14.42	<14.42	<14.50	<14.70	(9.0)	–			
	–6	18.08 ^{+0.24} _{–0.32}	18.35 ^{+0.12} _{–0.09}	16.92 ^{+0.34} _{–0.48}	15.79 ^{+1.01} _{–0.55}	14.30 ^{+0.35} _{–0.33}	18.54 ^{+0.11} _{–0.10}	6.6 ^{+0.7} _{–0.7}	7.5	107	125	259
Mrk116	–170	<14.37	<14.61	<14.33	<14.33	<14.27	<14.71	(9.0)	–			
	–39	<16.09	<15.41	<14.30	<14.29	<14.28	<15.01	(9.0)	–			
	9	18.73 ^{+0.11} _{–0.14}	18.58 ^{+0.14} _{–0.12}	17.30 ^{+0.29} _{–0.39}	16.40 ^{+0.48} _{–0.30}	14.84 ^{+0.40} _{–0.25}	18.97 ^{+0.09} _{–0.08}	7.9 ^{+0.6} _{–1.0}	–	67	145	243
Mrk153	–20	14.66 ^{+0.31} _{–0.23}	15.28 ^{+0.39} _{–0.29}	14.62 ^{+0.21} _{–0.21}	14.64 ^{+0.17} _{–0.16}	<14.16	15.51 ^{+0.27} _{–0.15}	9.7 ^{+3.3} _{–1.3}	9.0	222	364	(469)
	75	15.59 ^{+1.18} _{–0.76}	15.91 ^{+1.00} _{–0.49}	15.05 ^{+0.43} _{–0.22}	14.78 ^{+0.24} _{–0.15}	<14.53	16.14 ^{+0.88} _{–0.27}	8.5 ^{+1.5} _{–1.5}	6.9	116	246	(387)
Mrk205	–205	<13.94	<14.41	<14.16	<14.22	<14.07	<14.53	(9.0)	–			
	–48	<14.27	<14.59	<14.30	<14.55	<14.22	<14.69	(9.0)	–			

Table 3—Continued

object	$v(\text{H}_2)$ [km s ⁻¹]	$N(\text{J}=0)$	$N(\text{J}=1)$	$N(\text{J}=2)$	$N(\text{J}=3)$	$N(\text{J}=4)$	$N^a(\text{H}_2)$	W^b [km s ⁻¹]	W_f^c [km s ⁻¹]	T_{01}^d [K]	T_{23}^d [K]	T_{34}^d [K]
(1)	(2)	(3)	(4)	(5)	(6)	(7)	(8)	(9)	(10)	(11)	(12)	(13)
	-5	15.48 ^{+0.25} _{-0.21}	16.04 ^{+0.47} _{-0.26}	15.30 ^{+0.42} _{-0.24}	15.14 ^{+0.26} _{-0.21}	<14.13	16.23 ^{+0.35} _{-0.15}	11.5 ^{+1.5} _{-1.5}	11.0	188	281	(377)
	1281	14.89 ^{+0.23} _{-0.28}	15.57 ^{+0.38} _{-0.34}	14.90 ^{+0.17} _{-0.19}	14.90 ^{+0.16} _{-0.18}	<14.32	15.78 ^{+0.27} _{-0.18}	8.8 ^{+1.7} _{-0.6}	11.6	271	353	(429)
Mrk209	-99	<14.29	<14.51	<14.46	<14.52	<14.39	<14.62	(9.0)	-			
	-49	<14.77	<14.46	<14.46	<14.47	<14.37	<14.57	(9.0)	-			
	-9	<14.28	<14.52	<14.45	<14.47	<14.38	<14.63	(9.0)	-			
Mrk290	-138	<13.94	<14.22	<14.22	<14.16	<14.13	<14.36	(9.0)	-			
	-13	15.67 ^{+0.47} _{-0.35}	16.14 ^{+0.61} _{-0.44}	15.20 ^{+0.34} _{-0.22}	14.83 ^{+0.19} _{-0.16}	<14.16	16.31 ^{+0.49} _{-0.25}	10.1 ^{+1.0} _{-1.0}	11.0	153	221	(369)
Mrk335	-6	18.63 ^{+0.12} _{-0.12}	18.87 ^{+0.09} _{-0.10}	17.44 ^{+0.29} _{-0.65}	16.29 ^{+0.53} _{-0.39}	14.43 ^{+0.14} _{-0.11}	19.07 ^{+0.07} _{-0.07}	7.4 ^{+1.6} _{-1.4}	-	103	124	195
Mrk421	-60	13.31 ^{+0.20} _{-0.31}	13.75 ^{+0.18} _{-0.19}	<13.76	<13.79	<13.74	14.12 ^{+0.14} _{-0.15}	(9.0)	lin	144	(614)	(885)
	-19	13.87 ^{+0.16} _{-0.11}	14.47 ^{+0.26} _{-0.13}	13.89 ^{+0.19} _{-0.19}	14.00 ^{+0.18} _{-0.17}	<13.94	14.74 ^{+0.16} _{-0.07}	11.5 ^{+4.5} _{-4.5}	lin	209	428	(635)
Mrk477	-38	<14.84	<14.54	<14.49	<14.62	<14.39	<14.64	(9.0)	-			
	-5	<15.00	15.16 ^{+1.21} _{-0.36}	14.49 ^{+0.58} _{-0.30}	<14.72	<15.01	15.38 ^{+1.13} _{-0.27}	(9.0)	lin	(187)	(325)	(491)
Mrk501	-116	<14.46	<14.51	<14.57	<14.63	<14.63	<14.62	(9.0)	-			
	-83	<14.43	<14.54	<14.58	<14.63	<14.63	<14.64	(9.0)	-			
	2	14.60 ^{+0.64} _{-0.40}	15.26 ^{+0.85} _{-0.52}	14.61 ^{+0.45} _{-0.37}	14.64 ^{+0.31} _{-0.28}	<14.71	15.49 ^{+0.66} _{-0.24}	7.8 ^{+4.2} _{-1.3}	lin	252	371	(473)
Mrk509	-1	16.82 ^{+0.55} _{-0.40}	17.13 ^{+0.54} _{-0.38}	15.99 ^{+0.62} _{-0.35}	15.33 ^{+0.32} _{-0.19}	13.82 ^{+0.11} _{-0.17}	17.32 ^{+0.43} _{-0.23}	10.5 ^{+1.5} _{-1.5}	12.3	114	171	254
	60	13.75 ^{+0.17} _{-0.18}	14.33 ^{+0.18} _{-0.14}	13.85 ^{+0.14} _{-0.17}	14.09 ^{+0.15} _{-0.14}	<13.92	14.66 ^{+0.10} _{-0.07}	(9.0)	8.8	198	574	(657)
Mrk586	-11	15.25 ^{+0.55} _{-0.35}	15.67 ^{+0.76} _{-0.38}	14.81 ^{+0.37} _{-0.24}	14.53 ^{+0.25} _{-0.23}	<14.49	15.87 ^{+0.60} _{-0.21}	10.9 ^{+1.9} _{-1.9}	10.5	139	243	(418)
Mrk817	-109	<13.35	<13.61	<13.58	<13.51	<13.67	<13.83	(9.0)	-			
	-40	<13.79	13.59 ^{+0.11} _{-0.11}	<13.75	<13.54	<13.56	13.97 ^{+0.11} _{-0.11}	(9.0)	lin	(220)	(687)	(981)
	-5	13.65 ^{+0.11} _{-0.10}	14.19 ^{+0.14} _{-0.13}	13.61 ^{+0.10} _{-0.11}	13.76 ^{+0.12} _{-0.14}	<13.63	14.48 ^{+0.08} _{-0.07}	(9.0)	lin	179	464	(718)
Mrk876	-133	<13.71	<13.87	<13.84	<13.84	<13.95	<14.06	(9.0)	-			
	-30	14.76 ^{+0.60} _{-0.31}	15.26 ^{+0.51} _{-0.24}	14.51 ^{+0.31} _{-0.29}	14.39 ^{+0.28} _{-0.52}	<13.75	15.47 ^{+0.39} _{-0.15}	8.8 ^{+1.0} _{-1.0}	-	161	293	(476)
	-2	17.57 ^{+0.17} _{-0.21}	17.88 ^{+0.31} _{-0.41}	16.71 ^{+0.29} _{-0.29}	16.07 ^{+0.29} _{-0.27}	14.39 ^{+0.17} _{-0.23}	18.07 ^{+0.22} _{-0.22}	7.6 ^{+1.0} _{-0.5}	-	114	173	222
Mrk1095	9	18.65 ^{+0.13} _{-0.11}	19.03 ^{+0.12} _{-0.17}	17.87 ^{+0.18} _{-0.35}	17.09 ^{+0.51} _{-0.57}	14.94 ^{+0.25} _{-0.21}	19.20 ^{+0.08} _{-0.10}	10.7 ^{+2.8} _{-1.2}	-	130	157	162
Mrk1383	-2	13.80 ^{+0.13} _{-0.19}	14.54 ^{+0.31} _{-0.26}	13.94 ^{+0.20} _{-0.29}	14.03 ^{+0.20} _{-0.26}	<14.06	14.78 ^{+0.20} _{-0.14}	7.5 ^{+5.5} _{-1.5}	lin	346	412	(622)
Mrk1513	-25	14.57 ^{+0.28} _{-0.31}	14.89 ^{+0.26} _{-0.35}	14.16 ^{+0.21} _{-0.31}	14.08 ^{+0.19} _{-0.26}	<14.33	15.15 ^{+0.18} _{-0.17}	6.1 ^{+6.0} _{-0.5}	lin	117	313	(534)
	6	15.89 ^{+0.45} _{-0.20}	16.36 ^{+0.69} _{-0.27}	15.57 ^{+1.04} _{-0.43}	15.38 ^{+0.75} _{-0.37}	14.21 ^{+0.22} _{-0.24}	16.56 ^{+0.55} _{-0.15}	10.2 ^{+3.5} _{-2.5}	9.7	152	270	362
MS0700.7+6338	-1	18.61 ^{+0.10} _{-0.07}	18.90 ^{+0.07} _{-0.06}	17.36 ^{+0.24} _{-0.41}	16.04 ^{+0.33} _{-0.24}	14.21 ^{+0.27} _{-0.36}	19.09 ^{+0.05} _{-0.04}	7.3 ^{+0.8} _{-0.6}	-	113	113	198
NGC604	-240	14.26 ^{+0.22} _{-0.15}	14.83 ^{+0.24} _{-0.16}	14.28 ^{+0.16} _{-0.15}	14.46 ^{+0.21} _{-0.18}	<14.83	15.13 ^{+0.14} _{-0.08}	11.0 ^{+5.0} _{-3.0}	lin	193	496	(538)
	5	17.80 ^{+0.73} _{-1.05}	18.13 ^{+0.58} _{-1.14}	16.85 ^{+0.89} _{-1.03}	15.96 ^{+1.20} _{-0.80}	14.46 ^{+0.15} _{-0.14}	18.31 ^{+0.51} _{-0.47}	10.0 ^{+3.0} _{-2.0}	-	117	145	256
NGC625	0	<14.31	<14.74	<14.40	<14.31	<14.31	<14.82	(9.0)	-			
	396	14.69 ^{+0.72} _{-0.16}	15.10 ^{+0.60} _{-0.23}	14.39 ^{+0.32} _{-0.26}	14.40 ^{+0.25} _{-0.21}	<14.46	15.36 ^{+0.46} _{-0.12}	15.0 ^{+0.0} _{-0.0}	lin	136	358	(494)
NGC985	-2	15.43 ^{+0.68} _{-0.40}	15.89 ^{+0.92} _{-0.43}	14.98 ^{+0.40} _{-0.24}	14.60 ^{+0.25} _{-0.21}	<14.53	16.07 ^{+0.77} _{-0.24}	11.4 ^{+1.9} _{-1.9}	12.8	150	219	(395)
NGC1068	-58	<13.94	<14.12	<13.95	<14.03	<13.80	<14.27	(9.0)	-			

Table 3—Continued

object	$v(\text{H}_2)$ [km s ⁻¹]	$N(\text{J}=0)$	$N(\text{J}=1)$	$N(\text{J}=2)$	$N(\text{J}=3)$	$N(\text{J}=4)$	$N^a(\text{H}_2)$	W^b [km s ⁻¹]	W_f^c [km s ⁻¹]	T_{01}^d [K]	T_{23}^d [K]	T_{34}^d [K]
(1)	(2)	(3)	(4)	(5)	(6)	(7)	(8)	(9)	(10)	(11)	(12)	(13)
	5	17.67 ^{+0.41} _{-1.17}	17.82 ^{+0.39} _{-1.07}	16.62 ^{+0.58} _{-0.61}	15.89 ^{+0.60} _{-0.41}	<14.09	18.07 ^{+0.30} _{-0.43}	6.0 ^{+0.3} _{-0.3}	lin	91	162	(251)
NGC1399	-9	<14.27	<14.43	<14.50	<14.45	<14.43	<14.55	(9.0)	-			
NGC1522	0	<14.25	14.47 ^{+0.33} _{-0.23}	<14.48	<14.62	<14.39	14.74 ^{+0.33} _{-0.23}	(9.0)	lin	(202)	(429)	(636)
NGC1672	0	<14.49	<14.75	<14.46	<14.63	<14.51	<14.83	(9.0)	-			
NGC1705	-5	<13.68	<13.81	<13.82	<13.90	<13.78	<14.00	(9.0)	lin			
	88	<13.56	<13.80	<13.82	<13.92	<13.92	<14.00	(9.0)	-			
NGC3310	-47	18.32 ^{+0.51} _{-4.39}	18.79 ^{+0.33} _{-1.36}	15.76 ^{+0.32} _{-0.32}	15.14 ^{+0.33} _{-0.33}	14.18 ^{+0.19} _{-0.19}	18.88 ^{+0.30} _{-0.61}	7.0 ^{+2.0} _{-2.0}	7.0	104	104	104
	-17	18.19 ^{+0.44} _{-1.61}	18.61 ^{+0.39} _{-1.32}	15.75 ^{+0.33} _{-0.33}	15.31 ^{+0.32} _{-0.32}	<14.26	18.79 ^{+0.33} _{-0.58}	7.0 ^{+2.0} _{-2.0}	6.4	107	107	(107)
NGC3690	-100	<15.42	<14.28	<14.25	<14.19	<14.33	<14.41	(9.0)	-			
	-54	<14.22	<14.25	<14.24	<14.16	<14.32	<14.39	(9.0)	-			
	0	<16.50	<14.27	<14.18	<14.10	<14.20	<14.40	(9.0)	-			
NGC3783	-45	15.40 ^{+0.30} _{-0.10}	15.65 ^{+0.05} _{-0.10}	14.61 ^{+0.07} _{-0.08}	14.78 ^{+0.05} _{-0.06}	<13.89	15.52 ^{+0.12} _{-0.06}	(12.0)	lin	105	485	(402)
	-3	18.99 ^{+0.06} _{-0.07}	18.95 ^{+0.08} _{-0.05}	17.62 ^{+0.20} _{-0.29}	16.53 ^{+0.72} _{-0.43}	14.71 ^{+0.12} _{-0.09}	19.28 ^{+0.05} _{-0.04}	7.7 ^{+0.9} _{-0.9}	9.1	74	128	200
	62	<14.87	<14.44	<13.90	<13.87	<13.84	<14.55	(9.0)	-			
	244	17.67 ^{+0.55} _{-0.81}	18.00 ^{+0.45} _{-0.94}	16.60 ^{+0.41} _{-0.57}	15.49 ^{+0.20} _{-0.26}	14.00 ^{+0.11} _{-0.13}	18.17 ^{+0.38} _{-0.44}	8.2 ^{+1.2} _{-0.4}	8.2	117	127	259
NGC4051	-49	<14.30	14.43 ^{+0.50} _{-0.25}	<14.72	<14.30	<14.46	14.71 ^{+0.50} _{-0.25}	(9.0)	-	(203)	(436)	(645)
	-14	14.96 ^{+0.81} _{-0.42}	15.64 ^{+1.56} _{-0.66}	14.92 ^{+0.93} _{-0.37}	14.83 ^{+0.70} _{-0.28}	<14.55	15.83 ^{+1.37} _{-0.31}	6.9 ^{+1.5} _{-1.5}	lin	271	308	(423)
NGC4151	-21	15.94 ^{+0.59} _{-0.25}	16.42 ^{+0.68} _{-0.28}	15.53 ^{+0.65} _{-0.31}	15.24 ^{+0.23} _{-0.15}	14.06 ^{+0.07} _{-0.07}	16.60 ^{+0.54} _{-0.16}	11.5 ^{+1.8} _{-1.5}	11.8	156	240	357
NGC4214	-5	<14.66	14.85 ^{+0.44} _{-0.37}	14.30 ^{+0.27} _{-0.26}	14.46 ^{+0.28} _{-0.25}	<14.43	15.22 ^{+0.31} _{-0.19}	7.5 ^{+1.5} _{-1.5}	lin	(190)	346	(521)
NGC4449	-28	<14.57	<15.04	<14.57	<14.72	<14.28	<15.10	(9.0)	-			
NGC4449–HII	-28	13.88 ^{+0.14} _{-0.12}	14.54 ^{+0.28} _{-0.21}	13.98 ^{+0.21} _{-0.24}	14.18 ^{+0.18} _{-0.16}	<14.06	14.84 ^{+0.17} _{-0.10}	(9.0)	9.3	252	519	(606)
NGC4670	-8	14.14 ^{+0.29} _{-0.14}	14.62 ^{+0.56} _{-0.21}	14.07 ^{+0.36} _{-0.25}	14.27 ^{+0.28} _{-0.18}	<14.11	14.94 ^{+0.36} _{-0.10}	10.7 ^{+5.0} _{-5.0}	lin	156	519	(580)
NGC5236 ^d	-9	<13.98	14.52 ^{+0.18} _{-0.20}	<14.14	14.03 ^{+0.15} _{-0.21}	<14.12	14.79 ^{+0.14} _{-0.15}	9.0 ^{+6.0} _{-1.5}	lin	(201)	(418)	(620)
	500	14.42 ^{+0.29} _{-0.16}	15.02 ^{+0.36} _{-0.19}	14.39 ^{+0.20} _{-0.16}	14.46 ^{+0.17} _{-0.13}	<14.03	15.27 ^{+0.24} _{-0.10}	12.0 ^{+3.5} _{-3.5}	6.8	209	397	(511)
NGC5253 ^d	-4	14.85 ^{+0.11} _{-0.11}	15.52 ^{+0.11} _{-0.10}	14.95 ^{+0.11} _{-0.12}	15.11 ^{+0.12} _{-0.11}	14.25 ^{+0.13} _{-0.15}	15.80 ^{+0.06} _{-0.05}	11.2 ^{+3.0} _{-2.0}	14.1	261	475	590
	102	<14.11	<14.33	<14.22	<14.21	<14.21	<14.46	(9.0)	-			
	404	14.43 ^{+0.22} _{-0.14}	14.93 ^{+0.43} _{-0.25}	14.36 ^{+0.18} _{-0.16}	14.51 ^{+0.22} _{-0.17}	<14.28	15.23 ^{+0.27} _{-0.11}	10.0 ^{+3.0} _{-2.0}	lin	163	464	(519)
NGC5408	4	14.92 ^{+0.64} _{-0.36}	15.44 ^{+0.74} _{-0.43}	14.75 ^{+0.35} _{-0.26}	14.74 ^{+0.23} _{-0.21}	<14.61	15.67 ^{+0.56} _{-0.21}	16.0 ^{+9.0} _{-4.0}	lin	171	347	(444)
NGC7469	-333	<14.17	<14.78	<14.58	<14.18	<14.27	<14.86	(9.0)	-			
	-3	19.48 ^{+0.07} _{-0.07}	19.44 ^{+0.09} _{-0.07}	17.85 ^{+0.28} _{-0.74}	16.51 ^{+0.59} _{-0.38}	14.85 ^{+0.34} _{-0.21}	19.76 ^{+0.05} _{-0.04}	8.6 ^{+1.5} _{-1.5}	-	75	112	224
NGC7714	-316	<14.16	<14.38	<14.40	<14.26	<14.49	<14.50	(9.0)	-			
	-50	14.79 ^{+0.37} _{-0.17}	14.97 ^{+0.39} _{-0.16}	14.19 ^{+0.23} _{-0.19}	14.03 ^{+0.15} _{-0.18}	<14.26	15.26 ^{+0.27} _{-0.09}	11.2 ^{+0.0} _{-0.0}	11.3	96	281	(513)
	-5	18.55 ^{+0.07} _{-0.08}	18.70 ^{+0.07} _{-0.09}	17.30 ^{+0.17} _{-0.54}	16.21 ^{+0.27} _{-0.50}	14.61 ^{+0.25} _{-0.27}	18.94 ^{+0.05} _{-0.05}	5.8 ^{+1.5} _{-0.2}	-	93	128	236
PG0804+761	-58	<14.45	<15.24	<13.97	<14.10	<13.92	<14.66	(9.0)	-			
	-8	18.64 ^{+0.10} _{-0.11}	18.90 ^{+0.11} _{-0.12}	17.36 ^{+0.34} _{-0.41}	16.06 ^{+0.24} _{-0.23}	14.13 ^{+0.14} _{-0.16}	19.09 ^{+0.08} _{-0.08}	10.8 ^{+1.0} _{-1.3}	14.7	106	114	186

Table 3—Continued

object	$v(\text{H}_2)$ [km s ⁻¹]	$N(\text{J}=0)$	$N(\text{J}=1)$	$N(\text{J}=2)$	$N(\text{J}=3)$	$N(\text{J}=4)$	$N^a(\text{H}_2)$	W^b [kms ⁻¹]	W_f^c [kms ⁻¹]	T_{01}^d [K]	T_{23}^d [K]	T_{34}^d [K]
(1)	(2)	(3)	(4)	(5)	(6)	(7)	(8)	(9)	(10)	(11)	(12)	(13)
PG0844+349	6	18.09 ^{+0.12} _{-0.13}	18.37 ^{+0.12} _{-0.14}	16.73 ^{+0.38} _{-0.55}	15.36 ^{+0.41} _{-0.30}	<14.28	18.56 ^{+0.09} _{-0.09}	6.0 ^{+0.5} _{-0.5}	7.3	111	110	(231)
PG0953+414	-49	<13.56	<13.86	<14.00	<13.99	<14.07	<14.05	(9.0)	–			
	-26	14.05 ^{+0.23} _{-0.24}	14.66 ^{+0.41} _{-0.36}	14.00 ^{+0.18} _{-0.25}	13.97 ^{+0.22} _{-0.29}	<14.24	14.88 ^{+0.29} _{-0.18}	6.0 ^{+6.0} _{-1.0}	lin	215	337	(597)
	1	14.13 ^{+0.56} _{-0.19}	14.77 ^{+1.01} _{-0.30}	14.11 ^{+0.36} _{-0.21}	14.14 ^{+0.29} _{-0.23}	<14.12	15.00 ^{+0.81} _{-0.16}	6.9 ^{+3.0} _{-3.0}	7.2	236	371	(567)
PG1011–040	-5	17.73 ^{+0.12} _{-0.12}	18.10 ^{+0.15} _{-0.23}	16.59 ^{+0.30} _{-0.34}	15.52 ^{+0.23} _{-0.22}	<14.56	18.26 ^{+0.11} _{-0.15}	5.7 ^{+0.2} _{-0.2}	–	125	129	(243)
	123	<15.20	<14.28	<14.28	<14.29	<14.25	<14.41	(9.0)	–			
PG1116+215	-44	15.33 ^{+0.41} _{-0.33}	15.84 ^{+0.55} _{-0.38}	14.91 ^{+0.30} _{-0.22}	14.53 ^{+0.19} _{-0.17}	<14.12	15.27 ^{+0.44} _{-0.23}	12.2 ^{+0.8} _{-0.6}	6.6	142	246	(510)
	-11	<13.79	13.82 ^{+0.20} _{-0.22}	<13.91	<13.97	<13.90	14.17 ^{+0.20} _{-0.22}	(9.0)	lin	(215)	(595)	(860)
PG1211+143	-12	18.08 ^{+0.17} _{-0.17}	18.46 ^{+0.14} _{-0.16}	17.07 ^{+0.36} _{-0.57}	16.03 ^{+0.54} _{-0.34}	14.18 ^{+0.12} _{-0.12}	18.62 ^{+0.11} _{-0.11}	6.5 ^{+0.5} _{-0.5}	8.0	127	132	196
PG1259+593	-128	<13.87	<13.84	<13.66	<13.71	<13.98	<14.03	(9.0)	–			
	-54	13.31 ^{+0.18} _{-0.20}	13.88 ^{+0.16} _{-0.15}	<14.00	<14.06	<13.92	14.22 ^{+0.13} _{-0.12}	(9.0)	lin	193	(575)	(833)
	3	13.97 ^{+0.12} _{-0.12}	14.55 ^{+0.20} _{-0.19}	13.98 ^{+0.17} _{-0.20}	14.08 ^{+0.15} _{-0.17}	<13.93	14.82 ^{+0.12} _{-0.10}	8.0 ^{+7.0} _{-2.0}	lin	198	420	(613)
PG1302–102	-9	15.56 ^{+0.39} _{-0.31}	16.16 ^{+0.70} _{-0.45}	15.23 ^{+0.36} _{-0.26}	14.83 ^{+0.24} _{-0.20}	<14.34	16.30 ^{+0.58} _{-0.27}	8.9 ^{+0.7} _{-0.7}	9.3	209	215	(369)
PG1351+640	-156	<14.19	<14.62	<14.58	<14.39	<14.51	<14.72	(9.0)	–			
	-47	15.71 ^{+0.67} _{-0.99}	16.29 ^{+0.51} _{-0.01}	15.44 ^{+0.70} _{-0.79}	15.19 ^{+0.43} _{-0.59}	<14.61	16.46 ^{+0.42} _{-0.08}	6.3 ^{+8.0} _{-0.5}	6.9	196	252	(355)
	-2	17.88 ^{+0.23} _{-0.15}	18.13 ^{+0.14} _{-0.17}	17.03 ^{+0.35} _{-0.46}	16.33 ^{+1.73} _{-0.78}	14.36 ^{+0.22} _{-0.20}	18.34 ^{+0.20} _{-0.11}	7.8 ^{+1.5} _{-1.5}	11.0	106	166	181
PG1553+113	6	17.05 ^{+0.45} _{-0.74}	17.41 ^{+0.51} _{-0.70}	16.21 ^{+0.99} _{-1.11}	15.46 ^{+0.57} _{-0.64}	<14.59	17.58 ^{+0.41} _{-0.37}	7.3 ^{+4.2} _{-0.8}	7.2	125	160	(276)
PG1626+554	-121	<14.32	<14.49	<14.40	<14.45	<14.45	<14.60	(9.0)	–			
	-4	14.31 ^{+0.45} _{-0.37}	14.92 ^{+0.71} _{-0.38}	14.25 ^{+0.31} _{-0.34}	14.23 ^{+0.36} _{-0.36}	<14.58	15.14 ^{+0.54} _{-0.20}	9.5 ^{+5.5} _{-2.5}	6.0	215	342	(537)
PHL1811	0	19.05 ^{+0.10} _{-0.09}	19.07 ^{+0.12} _{-0.10}	17.51 ^{+0.29} _{-0.47}	16.18 ^{+0.35} _{-0.24}	14.71 ^{+0.13} _{-0.13}	19.36 ^{+0.07} _{-0.06}	9.4 ^{+0.4} _{-0.4}	–	79	113	262
PKS0405–12	4	15.28 ^{+0.35} _{-0.23}	15.79 ^{+0.40} _{-0.26}	15.07 ^{+0.23} _{-0.17}	14.99 ^{+0.19} _{-0.13}	14.08 ^{+0.12} _{-0.17}	16.01 ^{+0.28} _{-0.14}	11.2 ^{+1.0} _{-1.0}	11.3	167	313	535
PKS0558–504	1	14.81 ^{+0.42} _{-0.22}	15.41 ^{+0.54} _{-0.33}	14.66 ^{+0.26} _{-0.18}	14.52 ^{+0.23} _{-0.19}	<14.21	15.60 ^{+0.41} _{-0.18}	11.0 ^{+3.5} _{-2.5}	12.9	209	288	(456)
	71	<13.96	<14.15	<14.15	<14.16	<14.09	<14.30	(9.0)	–			
PKS2005–489	2	14.46 ^{+0.27} _{-0.18}	14.97 ^{+0.40} _{-0.24}	14.32 ^{+0.20} _{-0.21}	14.36 ^{+0.20} _{-0.21}	<14.26	15.22 ^{+0.27} _{-0.12}	10.6 ^{+4.0} _{-2.5}	10.7	167	377	(519)
PKS2155–304	-7	13.58 ^{+0.14} _{-0.15}	14.14 ^{+0.16} _{-0.14}	13.61 ^{+0.16} _{-0.24}	13.73 ^{+0.13} _{-0.15}	<13.70	14.42 ^{+0.09} _{-0.08}	(9.0)	8.3	188	437	(744)
TonS180	-6	<14.15	<14.35	<14.32	<14.32	<14.32	<14.47	(9.0)	–			
TonS210	-10	15.04 ^{+0.33} _{-0.30}	15.41 ^{+0.43} _{-0.35}	14.47 ^{+0.19} _{-0.19}	14.06 ^{+0.16} _{-0.22}	<14.11	15.61 ^{+0.32} _{-0.20}	8.1 ^{+1.7} _{-0.9}	7.3	127	213	(454)
VII Zw118	-3	18.60 ^{+0.08} _{-0.07}	18.91 ^{+0.07} _{-0.06}	17.48 ^{+0.23} _{-0.23}	16.35 ^{+0.54} _{-0.27}	14.41 ^{+0.24} _{-0.19}	19.09 ^{+0.05} _{-0.04}	8.1 ^{+1.0} _{-2.0}	–	116	125	185

Note. — a: FWHM values in Col. 9 that are in parentheses imply an FWHM of 9 kms⁻¹ was used to convert the equivalent width limits into column density limits. b: W_f is the FWHM fitted by combining all H₂ lines without damping wings, rather than by assuming that $T_{12} = T_{23}$. c: Temperature values in parentheses are not measured from observed column density ratios, but are expected values based on the correlations shown in Fig. 6. d: The listed errors for NGC 5236 and NGC 5253 do not include the systematic errors associated with the uncertain continuum placements. e: Sightlines where lines of $J=5$ are

detected: ESO 141–G55 – $\log N(5)=14.32_{-0.22}^{+0.17}$; HS 0624+6907 – $\log N(5)=14.67_{-0.25}^{+0.35}$; Mrk 116 – $\log N(5)=14.47_{-0.21}^{+0.22}$; Mrk 876 – $\log N(5)=13.94_{-0.12}^{+0.08}$; Mrk 1095 – $\log N(5)=14.53_{-0.20}^{+0.18}$; NGC 3783 – $\log N(5)=14.24_{-0.08}^{+0.10}$; NGC 4151 – $\log N(5)=13.45_{-0.25}^{+0.16}$; NGC 5253 – $\log N(5)=14.23_{-0.14}^{+0.13}$; NGC 7714 – $\log N(5)=14.17_{-0.32}^{+0.25}$; PG 1211+143 – $\log N(5)=13.98_{-0.11}^{+0.12}$; PHL 1811 – $\log N(5)=14.36_{-0.15}^{+0.12}$; PKS 0405–12 – $\log N(5)=14.05_{-0.19}^{+0.15}$

Table 4. H₂ outside the Milky Way Disk

object	cloud name	Published value			This paper		Note
		$v(\text{IVC})$ km s ⁻¹	$\log N(\text{H}_2)$	FWHM km s ⁻¹	$\log N(\text{H}_2)$	FWHM km s ⁻¹	
Intermediate-velocity H ₂ (compared to Richter et al. 2001).							
1H 0717+714	LLIV Arch	-51			14.96±0.18	9.0	new sightline
3C 273.0		+25	15.71	10.0	15.82±0.05	7.5	similar
Mrk 59	IV Arch	-44	14.72±0.28	6.8	15.03±0.14	linear	similar
Mrk 153					15.83±0.25	10.5	new sightline
Mrk 279	LLIV Arch	-41	<14.85		14.42±0.09	linear	additional data
Mrk 421	IV 26	-60	<14.93		14.12±0.18	linear	additional data
Mrk 509	complex gp	+60	14.92±0.46	9.2	14.67±0.06	9.0	similar
Mrk 817	IV Arch	-40	—		13.83±0.10	9.0	new detection
Mrk 876	Draco	-30	15.57±0.23	9.0	15.50±0.14	8.5	similar
Mrk 1513		-29	<16.43		15.16±0.11	linear	additional data
NGC 3310	IV Arch	-47	14.95±0.77	12.3	18.89±0.60	7.0	see Sect. 4.2
NGC 3783			—		15.59±0.06	12.0	no HI component
NGC 4051	IV 26	-49			14.71±0.19	linear	new sightline
NGC 4151	(IV 26)	-29	15.36±0.11	linear	16.61±0.10	11.5	low-velocity H ₂ @-21
NGC 7714	PP Arch	-50	<17.03		15.33±0.07	9.5	additional data
PG 1116+215	IV Spur	-42	15.27±0.34	13.2	16.01±0.14	6.5	<i>b</i> -value differs
PG 1259+593	IV Arch	-54	14.10±0.19	5.0	14.23±0.11	linear	similar
PG 1351+640	IV 19	-47	16.43±0.14	5.8	16.49±0.20	6.2	similar
H ₂ in high-velocity clouds (compared to Sembach et al. 2001a).							
NGC 3783	WW 187	240	16.80±0.10	20.0	18.17±0.40	8.2	<i>b</i> -value differs
Extragalactic H ₂ .							
Mrk 205	NGC 4319	1281			15.79±0.08	11.0	
NGC 604	in M 33	-240	<14.7		15.13±0.06	11.0	(Bluhm et al. 2003)
NGC 625		396			15.41±0.07	15.0	
NGC 5236	is M 83	500	15.2±0.3	25	15.27±0.07	12.0	(Hoopes et al. 2004)
NGC 5253		404	15.4±0.1	25	15.23±0.09	10.0	(Hoopes et al. 2004)